



# A spherical harmonics intensity model for 3D segmentation and 3D shape analysis of heterochromatin foci<sup>☆</sup>



Simon Eck<sup>a,\*</sup>, Stefan Wörz<sup>a</sup>, Katharina Müller-Ott<sup>b</sup>, Matthias Hahn<sup>c</sup>, Andreas Biesdorf<sup>a</sup>, Gunnar Schotta<sup>c</sup>, Karsten Rippe<sup>b</sup>, Karl Rohr<sup>a</sup>

<sup>a</sup>Biomedical Computer Vision Group, Department Bioinformatics and Functional Genomics, University of Heidelberg, IPMB, BioQuant, and German Cancer Research Center (DKFZ), 69120 Heidelberg, Germany

<sup>b</sup>Research Group Genome Organization and Function, BioQuant and German Cancer Research Center (DKFZ), 69120 Heidelberg, Germany

<sup>c</sup>Ludwig Maximilians University and Munich Center for Integrated Protein Science (CIPSM), Biomedical Center, 82152 Planegg-Martinsried, Germany

## ARTICLE INFO

### Article history:

Received 21 August 2015

Revised 7 March 2016

Accepted 9 March 2016

Available online 17 March 2016

### Keywords:

3D parametric intensity model

Spherical harmonics

Pericentric heterochromatin

Confocal light microscopy

## ABSTRACT

The genome is partitioned into regions of euchromatin and heterochromatin. The organization of heterochromatin is important for the regulation of cellular processes such as chromosome segregation and gene silencing, and their misregulation is linked to cancer and other diseases. We present a model-based approach for automatic 3D segmentation and 3D shape analysis of heterochromatin foci from 3D confocal light microscopy images. Our approach employs a novel 3D intensity model based on spherical harmonics, which analytically describes the shape and intensities of the foci. The model parameters are determined by fitting the model to the image intensities using least-squares minimization. To characterize the 3D shape of the foci, we exploit the computed spherical harmonics coefficients and determine a shape descriptor. We applied our approach to 3D synthetic image data as well as real 3D static and real 3D time-lapse microscopy images, and compared the performance with that of previous approaches. It turned out that our approach yields accurate 3D segmentation results and performs better than previous approaches. We also show that our approach can be used for quantifying 3D shape differences of heterochromatin foci.

© 2016 Elsevier B.V. All rights reserved.

## 1. Introduction

The genomic DNA of eukaryotic cells is packaged into chromatin, a large protein-DNA complex located inside the cell nucleus. Transcription, DNA replication, and DNA repair are examples of vital biological processes that depend on chromatin organization (Sexton et al., 2015, Cremer et al., 2015). In a coarse-grained classification, two functional states of chromatin are distinguished: the more open euchromatin active in transcription, and the more densely packed *heterochromatin* that is biologically inactive. Furthermore, formation of a stable heterochromatin structure is important for proper chromosome segregation and genomic stability, and its misregulation is linked to cancer and other diseases (Hahn et al., 2010, Plass et al., 2013). The establishment of heterochromatin is controlled by DNA methylation and post-translational histone modification, as well as the recruitment of architectural protein factors that recognize these so called epigenetic signals

(Saksouk et al., 2015). The quantitative analysis of the underlying regulatory epigenetic networks based on fluorescence microscopy images as well as other experimental readouts (Müller et al., 2009, Hathaway et al., 2012, Müller-Ott et al., 2014) is an emerging topic in biomedical science and medical diagnosis (Webster et al., 2013, Saab et al., 2014). A prototypic example of a transcriptionally silenced heterochromatic state is that of pericentric heterochromatin in mouse (Probst et al., 2008). It is ideally suited for a fluorescence microscopy image-based analysis. Due to their higher DNA content and enrichment of AT sequences, pericentric heterochromatic domains form condensed clusters that can be identified in mouse cells by staining with DAPI (4,6-diamidino-2-phenylindole), a fluorescent DNA-intercalating dye. Perturbances of the underlying epigenetic network are reflected in the structure and formation of pericentric heterochromatic domains. Furthermore, their shape changes during differentiation of embryonic stem cells and is functionally relevant for the pluripotent stem cell state (Meshorer et al., 2006, Mattout et al., 2015). Thus, there is a need to quantify heterochromatin and shape changes of heterochromatin domains in relation to cell differentiation, gene silencing, and chromosome segregation as well as to the misregulation of these processes in disease.

<sup>☆</sup> This paper was recommended for publication by Dr. James Duncan.

\* Corresponding author. Tel.: +49 6221 54 51305; fax: +49 6221 54 51488.

E-mail addresses: [simon.eck@bioquant.uni-heidelberg.de](mailto:simon.eck@bioquant.uni-heidelberg.de) (S. Eck), [s.woerz@dkfz.de](mailto:s.woerz@dkfz.de) (S. Wörz), [k.rohr@dkfz.de](mailto:k.rohr@dkfz.de) (K. Rohr).

<http://dx.doi.org/10.1016/j.media.2016.03.001>

1361-8415/© 2016 Elsevier B.V. All rights reserved.

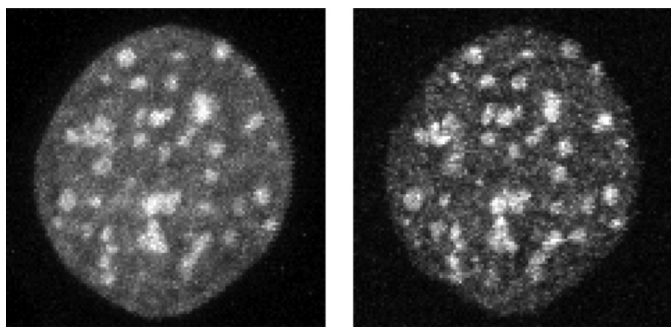


**Fig. 1.** Maximum intensity projections (MIPs) of a cell nucleus in a 3D two-channel microscopy image: DAPI-stained heterochromatin (left) and fluorescently labeled heterochromatin protein 1 $\alpha$  (HP1 $\alpha$ ) (right).

In this work, we address the task of heterochromatin quantification by introducing a novel approach for image analysis of heterochromatin domains in 3D fluorescence microscopy images. The pericentric heterochromatin regions studied here in mouse fibroblasts appear as bright fluorescent foci under the microscope (Fig. 1, left). To investigate heterochromatin formation and associated epigenetic mechanisms, these foci need to be accurately segmented and quantified. The formation process is connected with the dynamic recruitment of chromatin modifiers like the histone methyltransferases Suv39h1/h2 and Suv4-20h1/h2 or the heterochromatin protein 1 (HP1) isoforms (Hahn et al., 2013, Müller-Ott et al., 2014). To study the spatial and temporal dynamics of proteins in heterochromatin regions, *multichannel 3D images* showing foci of DAPI-stained DNA in one channel and foci of fluorescently labeled proteins in additional channels can be acquired (Fig. 1). Manual extraction of quantitative 3D information about foci, however, is difficult and highly time-consuming. On the other hand, computer-controlled microscopy systems enable to automate the acquisition of multichannel image data and can gather a large number of 3D images in short time (Pepperkok et al., 2006). Hence, automated image analysis approaches are required, which can extract the relevant information from multichannel 3D images by accurate 3D foci segmentation.

The automated segmentation of heterochromatin foci, however, is challenging for several reasons. In contrast to other subcellular structures (e.g., endoplasmic reticulum exit sites (Matula et al., 2010) or telomeres (Wörz et al., 2010, Osterwald et al., 2015)) the size and 3D shape of heterochromatin foci are subject to a high degree of variability. In particular, the 3D shape of foci can be highly irregular, thus standard geometric models like spheres or ellipsoids are not well suited for 3D shape representation. In addition, the appearance (intensity signal) of heterochromatin foci depends on the distribution of the staining dyes and is impaired by photon noise, non-uniform illumination, and by the blurring effect of the microscope described by the point spread function (PSF) (Waters et al., 2009). As a result, the intensity contrast of heterochromatin foci with respect to the nucleus background varies significantly and can be relatively low (Fig. 1). The latter issue is particularly relevant for the analysis of live cell microscopy images, where laser power needs to be kept to a minimum level to avoid photo-damaging the cells as well as bleaching the fluorescence signal during time course experiments. Hence, automatic approaches for 3D heterochromatin foci segmentation must cope with shape variations, non-homogeneous image intensities, as well as varying and low foci contrast.

In previous work, different methods were used for segmentation of heterochromatin foci from 3D fluorescence microscopy images. Often, global intensity thresholds are applied (e.g., Beil et al., 2002, Beil et al., 2005, Böcker et al., 2006, Jost et al., 2011, Ivashkevich et al., 2011, Cantaloube et al., 2012)), which are sensitive to intensity variations. Thus, approaches based on global thresholds are often combined with other techniques, such as the top-hat transform (Böcker et al., 2006, Ivashkevich et al., 2011, Cantaloube et al., 2012) or the H-dome transform (Ivashkevich et al., 2011) to improve the segmentation accuracy. Local thresholding within nuclei regions (Horáková et al., 2010, Eck et al., 2012) diminishes the effect of intensity variations between different nuclei, however, contrast variations between different foci in one nucleus are not addressed. In Andrey et al. (Andrey et al., 2010), Poulet et al. (Poulet et al., 2015), foci segmentation is performed by partitioning the nucleus into regions using the watershed transform and exclusion of low-contrast regions using manually defined thresholds. However, in the case of high levels of image noise or foci with low contrast, the watershed transform tends to over-segmentation. In Dzyubachyk et al. (Dzyubachyk et al., 2010), foci segmentation is performed by determining foreground voxels based on energy minimization using graph cuts within regions around the foci. However, as in the aforementioned approaches, segmentation is limited to the discrete voxel raster, and the blurring of the imaging process described by the microscope's PSF is not incorporated. In contrast, 3D parametric intensity models describe the shape and intensities of a structure by means of an analytic function, and allow incorporation of the image blurring as well as a priori information on foci appearance to improve the segmentation accuracy. For 3D segmentation, the model function is directly fitted to the image intensities within a 3D region-of-interest (ROI). Parametric intensity models were previously used for heterochromatin analysis (Eck et al., 2012) and analysis of other subcellular structures (Thomann et al., 2002, Wörz et al., 2010). However, there only regularly shaped models (e.g., spheres and ellipsoids) were used. Furthermore, 3D shape analysis of the foci was not considered, but provides additional insights into the heterochromatin formation process.

In this paper, we present a novel approach for accurate 3D model-based segmentation and 3D shape analysis of heterochromatin foci from multichannel 3D fluorescent microscopy images. Our approach employs a new 3D parametric intensity model, which is based on a *spherical harmonics* (SH) shape representation. Compared to previous intensity models, the new model enables to capture and analyze highly irregular 3D foci shapes. In previous work on 3D segmentation from biomedical images, different types of deformable models based on SH parametrization were used, for example, active shape models (Székely et al., 1996, Kelemen et al., 1996), statistical shape models (Kelemen et al., 1999, Tutar et al., 2006), and models combined with level set segmentation (Baust et al., 2010). Such approaches were used, for example, for the segmentation of brain structures from MR images (Székely et al., 1996, Kelemen et al., 1999) or the segmentation of cell nuclei (Kelemen et al., 1996, Marshall et al., 1996), however, 3D intensity models were not used and segmentation of heterochromatin or associated proteins was not considered. In this work, we use SH to formulate a 3D parametric intensity model, which describes both shape and intensities of heterochromatin foci. For 3D segmentation of heterochromatin foci in microscopy images, the proposed SH intensity model is directly fitted to the image intensities by least-squares minimization. Based on the segmentation result, the determined *SH expansion coefficients* are exploited for analyzing the 3D shape of the foci. SH shape analysis was previously used, for example, for brain structures in Gerig et al. (Gerig et al., 2001), Styner et al. (Styner et al., 2004), for lung nodules in El-Baz et al. (El-Baz et al., 2011), for cells in Khairy et al. (Khairy et al., 2010), Ducroz et al. (Ducroz et al., 2012), Du et al. (Du et al., 2013), and for cell nuclei in Singh et al. (Singh et al., 2011), however, approaches for characterizing the 3D shape of heterochromatin foci have not yet been introduced. Furthermore, the aforementioned approaches determine a

voxel-based (Styner et al., 2004, Khairy et al., 2010, Singh et al., 2011) or mesh-based (El-Baz et al., 2011, Ducroz et al., 2012) segmentation result, which is converted into a SH representation, often by employing the surface parametrization method proposed in Brechbühler et al. (Brechbühler et al., 1995). In our approach, such a conversion is not necessary since we directly obtain an analytic SH representation from segmentation by 3D model fitting. We demonstrate that 3D shape analysis based on the computed SH coefficients enables distinguishing different foci shapes and analyzing temporal shape changes. This work combines and extends our previous conference papers (Eck et al., 2013, Eck et al., 2014). Compared to that work, we have improved the automatic initialization of the model and use a Hessian-based multiscale approach for automatic estimation of a suitable 3D ROI for model fitting. Also, we describe the SH intensity model in more detail and present improvements on the computational efficiency. In addition, we have conducted a more comprehensive performance evaluation, in particular, we included a validation study based on 3D synthetic image data. We also successfully applied the approach to real 3D static and 3D dynamic image data and compared the results with previous approaches.

This paper is organized as follows. In Section 2, we introduce our 3D SH intensity model for representing the 3D shape and intensities of heterochromatin foci. Section 3 describes the approach for automatic 3D foci segmentation based on 3D model fitting. In Section 4, we present our approach for 3D shape analysis based on the SH expansion coefficients determined by model fitting. Experimental results for synthetic and real 3D image data are presented in Section 5. Finally, in Section 6 we discuss and conclude the work.

## 2. 3D spherical harmonics intensity model

In this section, we introduce a 3D spherical harmonics (SH) intensity model for analytic representation of the shape and intensities of heterochromatin foci in 3D microscopy images. First, we describe the 3D SH shape model (Section 2.1), and then we formulate a 3D SH intensity model (Section 2.2). The 3D SH intensity model provides the basis for both automatic 3D foci segmentation (Section 3) and 3D foci shape analysis (Section 4).

### 2.1. 3D spherical harmonics shape model

We represent the 3D shape of fluorescent foci using a spherical harmonics series expansion. Spherical harmonics (SH) form a complete set of basis functions defined on the sphere, enabling spherical functions to be expanded into a series of weighted SH. The complex-valued SH basis functions of degree  $l$  and order  $m$  are defined by (e.g., (Arfken et al., 2005))

$$Y_l^m(\theta, \varphi) = N_l^m P_l^m(\cos \theta) \cdot e^{im\varphi} \quad (1)$$

where  $P_l^m(\cdot)$  is an associated Legendre polynomial (see Appendix A),  $\theta \in [0, \pi]$  and  $\varphi \in [0, 2\pi)$  are the inclination and azimuth angles, respectively, and  $i = \sqrt{-1}$  is the imaginary unit. The normalization coefficients  $N_l^m = \sqrt{\frac{2l+1}{4\pi} \frac{(l-m)!}{(l+m)!}}$  are chosen such that the SH basis functions are orthonormal with respect to  $\theta$  and  $\varphi$  (Arfken et al., 2005). In our application, we assume the 3D region  $F$  of a fluorescent focus to be *star-shaped*, i.e., a point  $\mathbf{x}_0 \in F$  exists such that each ray originating from  $\mathbf{x}_0$  intersects the surface of  $F$  once. If  $\mathbf{x}_0$  is the origin of a spherical coordinate system, then the surface of  $F$  can be described by a 3D radius function  $r(\theta, \varphi)$ . Using (1),  $r(\theta, \varphi)$  can be written as a SH expansion of the form

$$r(\theta, \varphi, \mathbf{c}) = \sum_{l=0}^{\infty} \sum_{m=-l}^l c_l^m \cdot Y_l^m(\theta, \varphi) \quad (2)$$

where  $\mathbf{c} = (c_0^0, \dots, c_{\infty}^{\infty})^T$  denotes the vector of expansion coefficients, i.e., the weights of the SH basis functions. For more information about the mathematical foundations of SH and SH series expansion, see, for example, Courant and Hilbert (Courant et al., 1953), Arfken et al. (Arfken et al., 2005). Since the radius of foci is real-valued, we employ the real-valued SH basis functions (Courant et al., 1953)

$$Y_l^m(\theta, \varphi) = \begin{cases} \sqrt{2} N_l^m P_l^m(\cos \theta) \cos(m\varphi) & m > 0 \\ N_l^0 P_l^0(\cos \theta) & m = 0 \\ \sqrt{2} N_l^{|m|} P_l^{|m|}(\cos \theta) \sin(|m|\varphi) & m < 0. \end{cases} \quad (3)$$

Analogously, we distinguish between three cases of the expansion coefficients  $c_l^m$ :

$$c_l^m = \begin{cases} a_l^m & m > 0 \\ a_l^0 & m = 0 \\ b_l^m & m < 0. \end{cases} \quad (4)$$

Based on (3) and (4), and by defining a maximum series degree  $l_{\max}$ , the foci radius function  $r(\theta, \varphi)$  can be rewritten as the truncated real-valued SH expansion

$$r_{SH}(\theta, \varphi, \mathbf{a}, \mathbf{b}) = \sum_{l=0}^{l_{\max}} \left[ a_l^0 N_l^0 P_l^0(\cos \theta) + \sum_{m=1}^l \left( a_l^m \cos(m\varphi) + b_l^m \sin(m\varphi) \right) \times \sqrt{2} N_l^m P_l^m(\cos \theta) \right]. \quad (5)$$

In the remainder of the paper, we use the more compact notation  $r_{SH}(\theta, \varphi)$  for the SH shape model in (5). A specific 3D shape can be modeled by adjusting the coefficient vectors  $\mathbf{a} = (a_0^0, \dots, a_{l_{\max}}^{l_{\max}})^T$  and  $\mathbf{b} = (b_1^1, \dots, b_{l_{\max}}^{l_{\max}})^T$ . With increasing value of  $l_{\max}$ , the number of SH basis functions, given by  $(l_{\max} + 1)^2$ , also increases and more complex shapes can be described. Fig. 2 shows the influence of different coefficients on the SH shape model. In this example, we used  $a_0^0 = 10$  and the coefficients displayed below the subfigures, while all other coefficients were set to zero.

### 2.2. 3D parametric intensity model

The real-valued SH expansion in (5) describes the radius of a star-shaped object and can represent the 3D shape of a heterochromatin focus in confocal microscopy images. To include information about the signal intensities in the vicinity of a focus, we can formulate an ideal step-shaped 3D intensity model

$$g_{SH, ideal}(\mathbf{x}) = \begin{cases} 1 & \text{if } 0 \leq r \leq r_{SH}(\theta, \varphi) \\ 0 & \text{otherwise} \end{cases} \quad (6)$$

where  $\mathbf{x} = (x, y, z)^T$  denotes the 3D position and  $r = r(\mathbf{x})$  denotes the radius at  $\mathbf{x}$ . Note that  $g_{SH, ideal}$  is evaluated using Cartesian coordinates  $\mathbf{x}$ , thus facilitating the computation of the model intensity value at an image position for model fitting. The spherical parameters  $r$ ,  $\theta$ , and  $\varphi$  for computation of  $g_{SH, ideal}$  and  $r_{SH}(\theta, \varphi)$  are defined by

$$\begin{aligned} r(\mathbf{x}) &= \sqrt{x^2 + y^2 + z^2} \\ \theta(\mathbf{x}) &= \cos^{-1} \left( \frac{z}{r(\mathbf{x})} \right) \\ \varphi(\mathbf{x}) &= \tan^{-1} \left( \frac{y}{x} \right). \end{aligned} \quad (7)$$

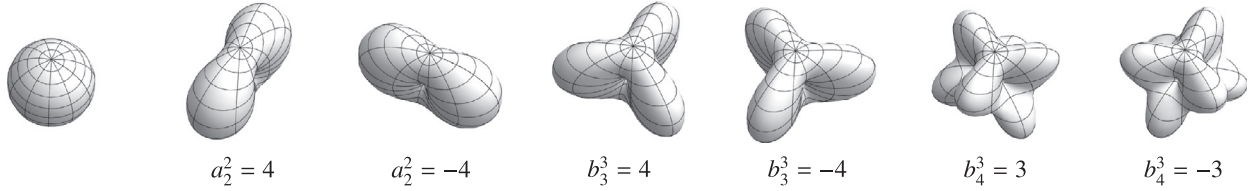


**Fig. 2.** Renderings of the 3D SH shape model demonstrating the shape influence of different SH coefficients. We used  $a_0^0 = 10$  and the coefficients displayed below the subfigures, while all other coefficients were set to zero.

However, the intensity profiles of heterochromatin foci in our image data cannot be well represented by an ideal step-shaped model. This is due to the blurring effect of the imaging process described by the PSF of the microscope. Previous work demonstrated that the 3D PSF of confocal microscopes can be well modeled by a 3D Gaussian function (e.g., (Thomann et al., 2002)). Hence, to represent the foci intensities more accurately, we use a convolution of  $g_{SH, ideal}$  with a 3D Gaussian function

$$G_{\sigma}^{3D}(\mathbf{x}) = \left( \frac{1}{\sqrt{2\pi}\sigma} \right)^3 \exp\left(-\frac{x^2 + y^2 + z^2}{2\sigma^2}\right), \quad (8)$$

specified by the standard deviation  $\sigma$ . Since a closed-form solution to the convolution of  $g_{SH, ideal}$  with a 3D Gaussian function  $G_{\sigma}^{3D}$  is not known, we approximate the solution using a convolution with a 1D Gaussian function  $G_{\sigma}^{1D}$  along 1D lines, which yields the 3D SH intensity model

$$g_{SH}(\mathbf{x}) = \Phi_{\sigma}(r + r_{SH}(\pi - \theta, \varphi + \pi)) - \Phi_{\sigma}(r - r_{SH}(\theta, \varphi)), \quad (9)$$

where  $\Phi_{\sigma}(x) = \Phi(\frac{x}{\sigma})$  is the Gaussian error function with

$$\Phi(x) = \int_{-\infty}^x G_{\sigma}^{1D}(\xi) d\xi = \int_{-\infty}^x \frac{1}{\sqrt{2\pi}} \exp\left(-\frac{1}{2}\xi^2\right) d\xi. \quad (10)$$

Consider a point  $\mathbf{x}$  where the model is evaluated, then  $g_{SH}$  represents the Gaussian smoothed 1D intensity profile along the line which intersects the model center and  $\mathbf{x}$  (see Fig. 3). The full width at half maximum (FWHM) of the intensity profile is given by the 3D coordinates  $(r_{SH}(\theta, \varphi), \theta, \phi)^T$  and  $(r_{SH}(\pi - \theta, \varphi + \pi), \pi - \theta, \varphi + \pi)^T$ , i.e., the intersection points of the line with the 3D surface of the heterochromatin focus. If  $\mathbf{x}$  is located close to the model center,  $g_{SH} \in [0, 1]$  is close to 1. If  $\mathbf{x}$  is located outside the FWHM (outside the surface),  $g_{SH}$  approaches zero. We further include a 3D translation  $\mathbf{x}_0 = (x_0, y_0, z_0)^T$  to model the global position of the foci within the image, as well as background and foreground intensity levels  $a_0$  and  $a_1$  to obtain the final 3D SH intensity model

$$g_{M,SH}(\mathbf{x}, \mathbf{p}) = a_0 + (a_1 - a_0)g_{SH}(\mathbf{x} - \mathbf{x}_0) \quad (11)$$

where  $\mathbf{p}$  represents the model parameter vector

$$\mathbf{p} = (\mathbf{a}, \mathbf{b}, a_0, a_1, \sigma, \mathbf{x}_0)^T. \quad (12)$$

The total number of model parameters depends on  $l_{max}$  and is given by  $|\mathbf{p}| = (l_{max} + 1)^2 + 6$ . In comparison to other parametric shape models (e.g., based on ellipsoids (Wörz et al., 2006)), additional parameters to represent, for example, rotation, bending, or tapering are not required, since the SH coefficients encode all shape information including the 3D orientation (see Fig. 2).

### 3. Automatic 3D foci segmentation

In this section, we describe how the spherical harmonics (SH) intensity model in (11) is utilized for 3D segmentation of heterochromatin foci. The segmentation approach is fully automatic and consists of four steps detailed below. First, 3D foci detection is performed to obtain coarse foci positions. Second, the size of the foci is estimated to determine the 3D region-of-interest (ROI) for

model fitting. Using the results of foci detection and ROI size determination, the 3D SH intensity model is initialized for each detected focus. By solving a least-squares minimization problem, the model is then fitted to the image intensities and optimal values of the model parameters are determined. Example results of different processing steps are shown in Fig. 4.

#### 3.1. 3D detection of heterochromatin foci

For automatic initialization of the 3D SH intensity model, we detect the position of heterochromatin foci by searching for local intensity maxima within  $7 \times 7 \times 7$  cubic ROIs. The size of the ROIs was chosen in accordance with the smallest foci in our 3D image data. Using larger ROIs generally increases the number of false negatives. We denoise the image beforehand using a 3D Gaussian filter with standard deviation  $\sigma_d$  and suppress background pixels with intensities below a clipping threshold. Since the foci contrast varies for different cell nuclei and images, an optimal clipping threshold for each cell nucleus is automatically computed based on the 3D intensity histogram  $h_i$  of the  $i$ th nucleus by  $T_{clip,i} = \mu_i + c_d \cdot \sigma_i$ , where  $\mu_i$  and  $\sigma_i$  denote the mean and standard deviation of  $h_i$ , respectively, and  $c_d$  is a constant. For the standard deviation of the Gaussian filter  $\sigma_d$  and the constant  $c_d$  we used fixed values for all images in an experiment (e.g., we used  $\sigma_d = 1.75$  and  $c_d = 1$  for the image in Fig. 4). Smaller values of  $\sigma_d$  and  $c_d$  lead to a better detection of small and dark foci and reduce the number of false negatives, however, more false positives occur if the values are chosen too small. In our experiments, we found a good compromise for  $\sigma_d$  and  $c_d$  based on visual inspection of the detection result for heterochromatin foci in several cell nuclei. To determine the 3D intensity histogram of a cell nucleus, we perform cell nucleus segmentation by 3D multilevel Otsu thresholding with prior 3D Gaussian filtering (we used a standard deviation of  $\sigma_{d,n} = 3$ ) and hole filling. To separate touching nuclei, we use a distance transform and a watershed transform. Example results of nucleus segmentation and foci detection are shown in Fig. 4b.

#### 3.2. Determination of 3D regions-of-interest for model fitting

The size of the 3D ROI used for model fitting influences the success of the fitting process and the segmentation accuracy. If the ROI is too large, neighboring foci can have a negative influence on the fitting result. If the ROI is too small (e.g., smaller than the heterochromatin focus itself), we might not include enough image information and model fitting may become unreliable. Since the size of the heterochromatin foci varies significantly, it is not appropriate to use a constant ROI size for all foci. In our previous work (Eck et al., 2013, Eck et al., 2014), we addressed this by repeated model fitting using a range of different ROIs (starting from a user defined minimum ROI radius), and used the segmentation result of the smallest ROI for which model fitting was successful. However, in the case of the SH intensity model, this scheme does not always yield good segmentation results. Hence, we propose a different strategy based on a multiscale approach, which yields more

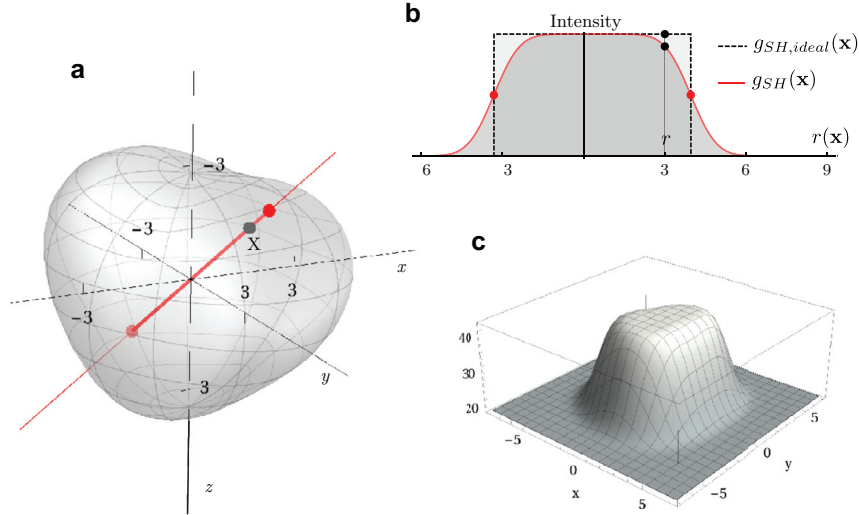


**Fig. 3.** Example of a 3D parametric intensity model computed from a real 3D microscopy image: (a) 3D shape model, (b) 1D intensity profile along the line shown in (a) without (dashed) and with convolution (solid) with a Gaussian function, as well as (c) 2D intensity profile of the  $xy$ -plane at  $z = 0$ .

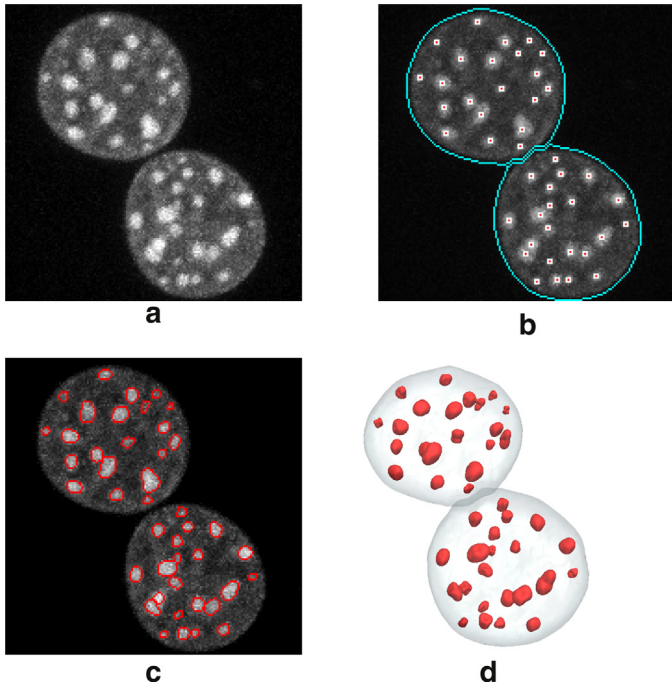


**Fig. 4.** Automatic 3D segmentation results shown as maximum intensity projections (MIPs): (a) Original 3D microscopy image of a mouse embryonic fibroblast cell nucleus with DAPI staining, (b) results of cell nucleus segmentation (blue contour) and spot detection (dots), (c) 3D foci segmentation results by 3D SH intensity model fitting, and (d) rendering of 3D nucleus and 3D foci segmentation results.

accurate segmentation results. The approach was previously used in Frangi et al. (Frangi et al., 1998) for enhancement of tubular structures in medical image data, and in Jaeger et al. (Jaeger et al., 2010) for blob detection in microscopy images of subcellular structures. Here, we utilize the approach to determine a suitable ROI for model fitting based on the size of a heterochromatin focus using the intensity information in the neighborhood of the detected focus position. To analyze the image intensities  $g(\mathbf{x})$ , we compute the Hessian matrix  $\mathcal{H}(g, \sigma_s)(\mathbf{x})$  for the scale  $\sigma_s$ . For calculating the required second order partial derivatives in  $\mathcal{H}(g, \sigma_s)(\mathbf{x})$ , we use convolutions with Gaussian derivative filters. For example, for the first

element we use

$$g(\mathbf{x}) * \frac{\partial^2}{\partial x^2} G_{\sigma_s}^{3D}(\mathbf{x}) \quad (13)$$

with the 3D Gaussian function  $G_{\sigma_s}^{3D}(\mathbf{x})$  in (8). We then compute the ratio

$$B(\mathbf{x}, \sigma_s) = \frac{|\lambda_3(\mathbf{x}, \sigma_s)|}{\sqrt{|\lambda_1(\mathbf{x}, \sigma_s)\lambda_2(\mathbf{x}, \sigma_s)|}} \quad (14)$$

where  $\lambda_k$  denotes the  $k$ th eigenvalue of the Hessian matrix sorted by their magnitude in descending order ( $|\lambda_1| \geq |\lambda_2| \geq |\lambda_3|$ ) (Frangi et al., 1998).  $B(\mathbf{x}, \sigma_s)$  is large if the 3D neighborhood of  $\mathbf{x}$  forms a blob-like structure with a radius of about  $\sigma_s$ . In our case, the radius of a heterochromatin focus is determined as the scale  $\sigma_s$  for which  $B(\mathbf{x}, \sigma_s)$  is maximal. However,  $\sigma_s$  is not a good choice for the size of the ROI, since the model represents foreground as well as background intensities, and therefore model fitting is more accurate for larger ROIs which contain more image background. A better choice is using a ROI radius which is twice as large as  $\sigma_s$  and can be computed by

$$\hat{R}_{ROI} = \arg \max_{R_{\min} \leq R \leq R_{\max}} B\left(\mathbf{x}, \frac{R}{2}\right) \quad (15)$$

where  $\hat{R}_{ROI}$ ,  $R_{\min}$ , and  $R_{\max}$  are integer values given in voxels.  $R_{\min}$  and  $R_{\max}$  are chosen based on the expected range of foci sizes and remain fixed for all images in an experiment (e.g., we used  $R_{\min} = 4$  and  $R_{\max} = 11$  for the image in Fig. 4). To account for the typical anisotropic resolution in microscopic image data (in confocal microscopy images, the resolution in  $z$ -direction is typically lower than within the  $xy$ -plane), we scale  $\hat{R}_{ROI}$  in  $z$ -direction according to the voxel resolution, so that the same physical sizes are considered. We thus use a fitting ROI of ellipsoidal shape with semi-axes  $\hat{\mathbf{R}}_{ROI} = (\hat{R}_{ROI}, \hat{R}_{ROI}, v_{xz}\hat{R}_{ROI})^T$ , where  $v_{xz}$  is the ratio between the physical voxel sizes in  $x$ - and  $z$ -direction. Note that compared to Frangi et al. (Frangi et al., 1998) and Jaeger et al. (Jaeger et al., 2010), where the Hessian-based analysis is performed for each voxel, in our approach we analyze the image intensities only at the detected foci positions which significantly reduces the computation time.

### 3.3. Model initialization

The parameter vector  $\mathbf{p}$  in (12) of the SH intensity model is automatically initialized in the following way. The translation

parameters  $\mathbf{x}_0$  are initialized using the detected foci positions (see Section 3.1). The size and 3D shape of the model are controlled by the SH coefficients  $a_l^m$  and  $b_l^m$ . We initialize the model with the shape of a sphere by setting all SH coefficients to zero except  $a_0^0$ , which determines the radius of the sphere (the radius is given by  $N_0^0 a_0^0$ ). To initialize  $a_0^0$ , we use the estimated size of the foci (see Section 3.2). The parameter  $\sigma$  is initialized based on the blurring observed in the image data. We used  $\sigma \in [0.5, 1.0]$  in our experiments. The foreground intensity  $a_1$  is initialized with the maximal intensity value within a radius of two voxels around the detected focus position  $\mathbf{x}_0$ . We found that using the maximal intensity value is more robust to image noise than, for example, using the intensity value at the detected focus position. The background intensity  $a_0$  is initialized with the minimal intensity value within the fitting ROI.

### 3.4. 3D least-squares model fitting

To determine the model parameters  $\mathbf{p}$  in (12), the 3D SH intensity model  $g_{M,SH}(\mathbf{x}, \mathbf{p})$  in (11) is directly fitted to the image intensities  $\mathbf{g}(\mathbf{x})$  by solving a least-squares minimization problem. In contrast to other approaches using SH models, our approach does not require additional image features (e.g., image gradients (Székely et al., 1996, Kelemen et al., 1996) or region-based terms (Baust et al., 2010)) to estimate the model parameters. Instead, we directly exploit the intensity information within ellipsoidal ROIs at the detected positions of the foci, using the objective function

$$\chi^2(\mathbf{p}) = \sum_{\mathbf{x} \in \text{ROI}} (g_{M,SH}(\mathbf{x}, \mathbf{p}) - \mathbf{g}(\mathbf{x}))^2 \rightarrow \min. \quad (16)$$

For minimization we use the method of Levenberg and Marquardt (Marquardt et al., 1963) which incorporates first order partial derivatives of  $g_{M,SH}$  with respect to the model parameters  $\mathbf{p}$ . All partial derivatives of  $g_{M,SH}$  have been derived analytically and are provided in Appendix B. The minimization is performed for each detected heterochromatin focus. For large values of  $l_{\max}$ , fitting all model parameters  $\mathbf{p} = (\mathbf{a}, \mathbf{b}, a_0, a_1, \sigma, \mathbf{x}_0)^T$  at once can render the fitting process unstable. In addition, it is advantageous for 3D shape analysis if a geometric reference point such as the center of mass  $\mathbf{x}_m$  is used for the model center  $\mathbf{x}_0$  (see also Section 4). To improve the robustness of model fitting and to align  $\mathbf{x}_0$  with  $\mathbf{x}_m$ , we use a stepwise procedure for estimating the model parameters which consists of multiple fitting phases. In the first phase, we estimate the position  $\mathbf{x}_0$  and the SH coefficients up to the second degree, while fixing all other parameters. This allows translation, scaling, and low-frequency shape deformations of the model and yields a first approximation of the 3D shape of a focus. In the second phase, we additionally estimate the intensity parameters  $a_0$  and  $a_1$  and the higher-degree SH coefficients to allow more complex shape deformations of the model and to accurately capture the 3D shape of a focus. Fig. 5 demonstrates how the 3D shape evolves during the first and second fitting phase for a heterochromatin focus in a real 3D image. Based on the result of the second phase, we compute  $\mathbf{x}_m$  and set  $\mathbf{x}_0$  to  $\mathbf{x}_m$ . We then repeat the second fitting phase while fixing  $\mathbf{x}_0$ . In the final fitting phase, we

determine the smoothing parameter  $\sigma$  while fixing all other parameters.

### 3.5. Improvement of the computation time

In the following, we describe improvements of the proposed approach which reduce the computation time. For model fitting according to (16), in each iteration of the minimization, the 3D SH intensity model in (11) is evaluated at every position  $\mathbf{x}$  of the 3D ROI. In a typical example, the minimization requires 25 iterations and a ROI with semi-axes  $\hat{\mathbf{R}} = (10, 10, 7)^T$  is used, and thus (11) is evaluated about 80,000 times. To reduce the computation time we can exploit the fact that the normalization coefficients  $N_l^m$  in (5) do not depend on  $\mathbf{x}$  and thus can be computed in advance. In addition, for efficient computation of the higher-order associated Legendre polynomials  $P_l^m(x)$  in (5), well-known recurrence formulas can be used (e.g., (Arfken et al., 2005)). Likewise,  $\sin(m\varphi)$  and  $\cos(m\varphi)$  in (5) can be efficiently computed for  $m > 2$  using the following trigonometric relations (recurrence formulas for Chebyshev polynomials and related relations in, e.g., (Arfken et al., 2005))

$$\begin{aligned} \cos(mx) &= 2 \cos x \cdot \cos((m-1)x) - \cos((m-2)x), \\ \sin(mx) &= 2 \cos x \cdot \sin((m-1)x) - \sin((m-2)x) \end{aligned} \quad (17)$$

Note that (17) only reduces the computational cost for  $l_{\max} > 2$ , however, in real scenarios with  $l_{\max} \in [4, 6]$  we already achieve about 10% reduction of the computation time. Moreover, in (9) and (5), the relations

$$\cos(m(\varphi + \pi)) = \begin{cases} -\cos(m\varphi) & \text{if } m \text{ is odd} \\ \cos(m\varphi) & \text{if } m \text{ is even} \end{cases} \quad (18)$$

and analogous for  $\sin(m(\varphi + \pi))$ , as well as

$$P_l^m(\cos(\pi - \theta)) = \begin{cases} -P_l^m(\cos \theta) & \text{if } (l+m) \text{ is odd} \\ P_l^m(\cos \theta) & \text{if } (l+m) \text{ is even} \end{cases} \quad (19)$$

can be used. Overall, using the improvements in (17), (18), and (19), we achieve a reduction of the computation time of about 25%.

## 4. 3D foci shape analysis

In this section, we describe how the 3D shape of heterochromatin foci can be analyzed based on the 3D SH intensity model  $g_{M,SH}$  in (11). By fitting the 3D SH intensity model to the image data, the SH coefficients  $a_l^m$  and  $b_l^m$  are automatically determined. Depending on the degree  $l$ , the coefficients  $a_l^m$  and  $b_l^m$  control the influence of the SH basis functions of different frequencies and thus contain information about the frequency components which determine the 3D shape of the fitted heterochromatin focus (see also Fig. 2). However, the 3D shape of a focus can be well represented by different combinations of  $a_l^m$ ,  $b_l^m$ , and the model center  $\mathbf{x}_0$ . For example,  $\mathbf{x}_0$  could be chosen at the center of mass or at the border of a focus, and for both cases different coefficients  $a_l^m$  and  $b_l^m$  exist that well represent the focus. To avoid such ambiguity, we use the center of mass  $\mathbf{x}_m$  for the model center  $\mathbf{x}_0$  (see also Section 3.4). Furthermore, the values of  $a_l^m$  and  $b_l^m$  depend on the

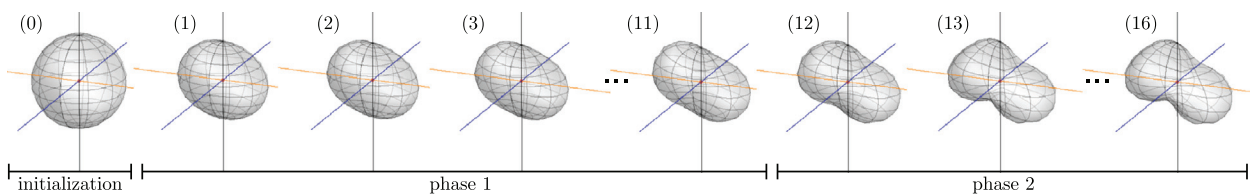
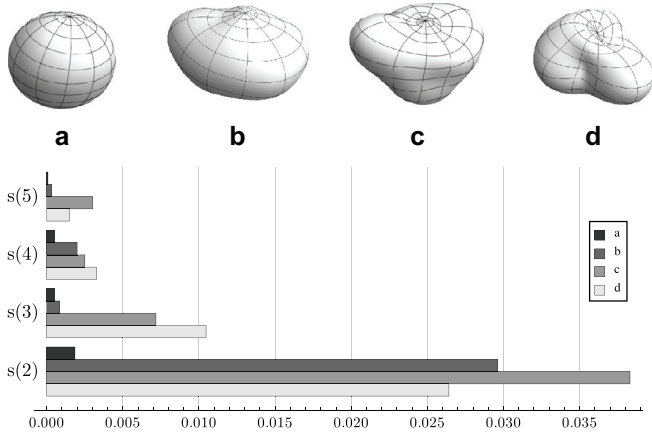
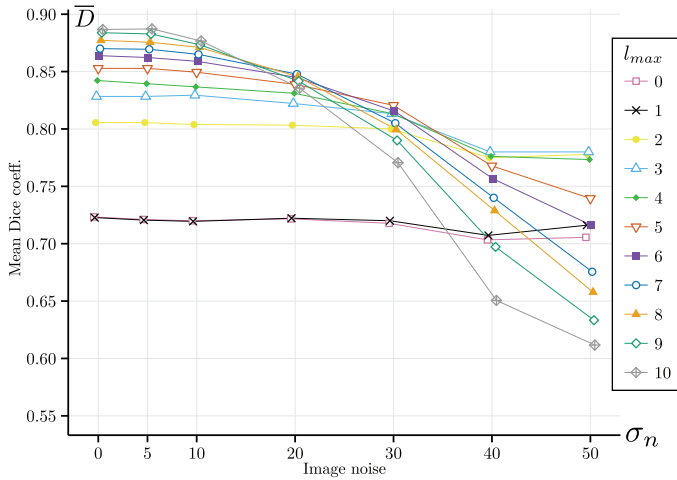


Fig. 5. Evolution of the shape of the 3D SH intensity model as a function of the iteration of the model fitting process for a heterochromatin focus in a real 3D image. The initial shape is shown on the left (iteration 0). Iterations 1 to 11 belong to the first fitting phase, and iterations 12 to 16 belong to the second fitting phase.



**Fig. 6.** Heterochromatin foci from real 3D microscopy images and bar plot of the shape descriptor  $s(l)$  for different SH degrees  $l = 2, 3, 4, 5$ . (a-d) show the 3D shapes of (a) a focus with sphere-like shape, (b) a focus with ellipsoid-like shape, and (c) and (d) foci with more complex shapes.



**Fig. 7.** Segmentation results of the proposed approach for synthetic 3D image data: Mean Dice coefficient  $\bar{D}$  (averaged over all 18 foci) as a function of the image noise level  $\sigma_n$ , and different maximum series degrees  $l_{max}$  for the SH intensity model.

size and rotation of a focus. To solely describe 3D shape properties, and to enable shape comparison between different foci, we use a *SH shape descriptor* for  $g_{M, SH}$  which reads as

$$s(l) = \sum_{m=0}^l |\hat{a}_l^m|^2 + \sum_{m=1}^l |\hat{b}_l^m|^2 \quad (20)$$

where  $\hat{a}_l^m = a_l^m/a_0^0$  and  $\hat{b}_l^m = b_l^m/a_0^0$  are the size normalized SH coefficients, i.e.,  $\hat{a}_l^m$  and  $\hat{b}_l^m$  do not change when changing the size of  $g_{M, SH}$ .  $s(l)$  denotes the energy of the SH function at different degrees  $l$ . Since this energy does not change when  $g_{M, SH}$  is rotated,  $s(l)$  is a rotationally invariant shape descriptor (Kazhdan et al., 2003, Gu et al., 2004). Thus,  $s(l)$  does not depend on the size and rotation of a focus.

For each heterochromatin focus  $f$ , we compute the vector  $\mathbf{s}_f = \{s_f(1), s_f(2), \dots, s_f(l_{max})\}$  consisting of values of the shape descriptor  $s(l)$  for different degrees  $l$ . Heterochromatin foci with a sphere-like shape have relatively small values of  $s(l)$ . Foci with an ellipsoid-like shape have large values for  $s(2)$ . Foci with more complex shape characteristics have relatively large values of  $s(l)$  for  $l \in [2, l_{max}]$ , and hence can be distinguished from foci with simpler shape. Fig. 6 shows examples of 3D shapes and corresponding values of  $s(l)$  for four foci from real 3D microscopy image data.

## 5. Experimental results

To analyze the performance of our approach, we used 3D synthetic and 3D real static image data, as well as 3D real dynamic time-lapse images.

### 5.1. Synthetic 3D image data

We generated the 3D images for our synthetic experiments based on manual binary segmentations of heterochromatin by biological experts. This has the advantage that realistic 3D shapes are employed. We used 18 foci with different size and shape characteristics. The foreground and background intensities of the synthetic data were set to  $a_1 = 100$  and  $a_0 = 30$ , respectively. To simulate the blurring of the imaging system, we applied a 3D Gaussian filter with standard deviation  $\sigma = 0.75$  which yields an intensity profile typical for the heterochromatin foci in our real 3D image data. In addition, to evaluate the robustness of our approach to image noise, we used different levels of additive Gaussian noise specified by the standard deviations  $\sigma_n = 0, 5, 10, 20, 30, 40, 50$ . The corresponding signal-to-noise ratios (SNRs) are given by  $SNR = (a_1 - a_0)/\sigma_n = \infty, 14.0, 7.0, 3.5, 2.3, 1.8, 1.4$ . In total, we used 126 synthetic 3D images.

In the first synthetic experiment, we examined how the choice of the parameter  $l_{max}$  (which specifies the maximum SH degree and thus the overall number of model parameters) affects the segmentation performance of our approach. As  $l_{max}$  increases, the SH intensity model can represent more shape details but model fitting becomes less robust and computationally more expensive. As performance measure we used the Dice coefficient  $D(G, S) = 2|G \cap S|/|G| + |S|$ , where  $G$  and  $S$  denote the binary volumes of the synthetic ground truth and the segmentation result, respectively. Fig. 7 shows the mean Dice coefficient  $\bar{D}$  (averaged over all considered 18 foci) as a function of the noise level  $\sigma_n$ . Our results show that  $\bar{D}$  is relatively low if  $l_{max} \leq 3$ , because foci with complex 3D shape cannot be represented well. In contrast, higher values of  $l_{max}$  allow representing more shape details and yield better results for low noise levels ( $\sigma_n \leq 20$ ), however, for  $l_{max} \geq 7$ ,  $\bar{D}$  decreases significantly for high noise levels ( $\sigma_n \geq 30$ ). Hence, we identified  $l_{max} = 4, 5, 6$  as a good choice for most foci in our experiments, since a relatively high accuracy is obtained and the result is relatively stable for high noise levels. For relatively small foci (volume smaller than 200 voxels),  $l_{max} = 3$  is a good choice, because such foci generally exhibit few shape details and a relatively small ROI is used for fitting.

In the second experiment, we compared the results of our approach using  $l_{max} = 5$  with three other approaches: 1) 3D Gaussian model fitting (Wörz et al., 2010) (GAUSS); 2) multiscale decomposition using undecimated wavelet transform and thresholding of the wavelet bands (Olivo-Marin et al., 2002) (UDWT) implemented in the software Icy (de Chaumont et al., 2012), which was previously used, for example, for segmentation of endosomes or centrosomes in cells (Pop et al., 2013); and 3) top-hat transform and Yen thresholding Yen et al. (Yen et al., 1995) (TH+Y), which was proposed for segmentation of heterochromatin foci in Cantaloube et al. (Cantaloube et al., 2012). Our approach based on the SH intensity model is denoted as SHIM in the following. Since TH+Y yielded a relatively large number of false positives and holes within the foci volumes, foci smaller than 15 voxels were excluded and hole filling was applied to improve the segmentation.

Fig. 8 shows for all approaches maximum intensity projections (MIPs) of the 3D segmentation results for one focus for different noise levels  $\sigma_n$ . Fig. 9 gives the mean Dice coefficients  $\bar{D}$  (averaged over all 18 foci) as a function of  $\sigma_n$ . Our results show that GAUSS is robust to noise, however, it fails to capture fine shape details and thus yields smaller values of  $\bar{D}$  compared to the other approaches

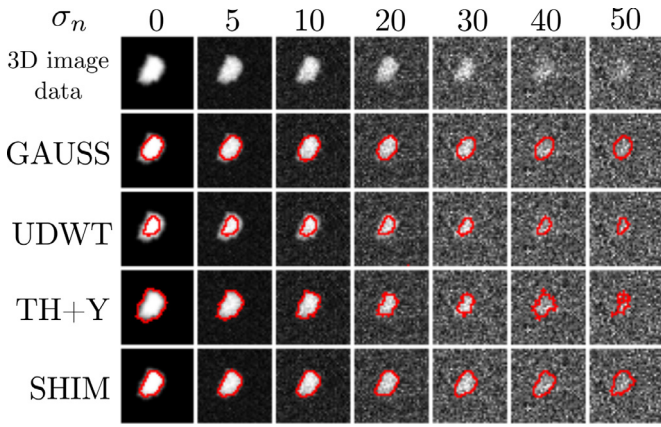


**Fig. 8.** Maximum intensity projections (MIPs) of synthetic 3D data with different image noise levels  $\sigma_n$  and segmentation results of 3D Gaussian model fitting (GAUSS), multiscale decomposition using undecimated wavelet transform (UDWT), top-hat filtering and Yen thresholding (TH+Y), and our approach based on the SH intensity model (SHIM).

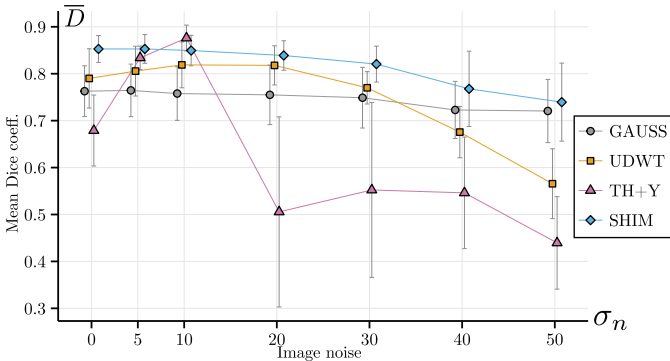


**Fig. 9.** Segmentation results of different approaches for synthetic 3D image data as a function of the image noise level  $\sigma_n$ : Mean Dice coefficient  $\bar{D}$  (averaged over all 18 foci) obtained by 3D Gaussian model fitting (GAUSS), multiscale decomposition using undecimated wavelet transform (UDWT), top-hat filtering and Yen thresholding (TH+Y), and our approach based on the SH intensity model (SHIM).

for low noise levels ( $\sigma_n < 20$ ). TH+Y yields relatively good values for low noise levels, but  $\bar{D}$  degrades significantly for  $\sigma_n \geq 20$ . UDWT yields relatively good results for most foci if  $\sigma_n \leq 30$ , however, the volume of some relatively large foci is underestimated, and  $\bar{D}$  degrades for  $\sigma_n > 30$ . SHIM yields the best overall result, it can cope well with shape details, and relatively large values of  $\bar{D}$  for all noise levels are obtained.

## 5.2. Real 3D static microscopy image data

We also applied our approach to real 3D static microscopy images of mouse embryonic fibroblast cells from two experiments. In the first experiment, we evaluate the segmentation performance of our approach for heterochromatin foci in two-channel 3D image data. In the second experiment, we investigate our approach for 3D shape characterization of foci from different cell lines.

### 5.2.1. Automatic segmentation of heterochromatin foci in two-channel 3D image data

We applied our approach to 524 real 3D two-channel microscopy images ( $512 \times 512 \times 41$  voxels). Foci in the DAPI channel mark DNA-dense regions (i.e., pericentric heterochromatin) and foci in the HP1 $\alpha$  channel mark high concentrations of heterochromatin protein 1 $\alpha$  (Fig. 1). To cope with the strongly varying size of the foci, we distinguish between small and large foci and use a

series degree  $l_{max}$  of 3 and 5, respectively. For comparison, we also applied two other approaches based on parametric intensity models: GAUSS and an approach based on a combination of region-adaptive segmentation and 3D Gaussian model fitting (Eck et al., 2012) (RA+GA). For small foci, GAUSS yielded relatively good results, however, it fails to accurately segment large foci of irregular shape. RA+GA generally yields decent results, but does not cope well with intensity inhomogeneities in the cell nucleus, e.g., relatively dark foci pixels were not segmented. In comparison, our approach based on the 3D SH intensity model (SHIM) copes well with foci of different sizes and highly irregular shapes and yields a better overall result. We also compared the results to the UDWT and the TH+Y approach. As for the synthetic experiments, exclusion of small foci and hole filling was performed for TH+Y. The results after these additional steps were relatively good for most foci, however, over- and under-segmentation occurred in the case of high image noise. UDWT yielded good results, but segmentation was less accurate compared to RA+GA and SHIM. Fig. 10 shows examples for the results of all 3D segmentation approaches in the HP1 $\alpha$  and DAPI channels.

To quantify the segmentation accuracy, we computed the Dice coefficient between the 3D segmentation results and expert ground truth. We also computed the Hausdorff distance

$$H(G, S) = \max\{h(G, S), h(S, G)\},$$

$$h(G, S) = \max_{g \in G} \min_{s \in S} \|g - s\|$$

where  $G$  and  $S$  denote the binary volumes of the expert ground truth and the segmentation result, respectively,  $g$  denotes an image position inside  $G$ , and  $s$  denotes an image position inside  $S$ . To establish the ground truth, two expert observers manually segmented 243 foci volumes from four two-channel 3D images. For each automatic approach we experimentally determined a best set of parameters and used them for the whole data. Mappings between the foci in the ground truth and the automatic results were determined in 3D based on the minimum distance of the centers of mass. Table 1 shows mean values  $\bar{D}$  and standard deviations  $\sigma_D$  of the Dice coefficient  $D$  for foci in the HP1 $\alpha$  and DAPI microscopy channel as well as for all foci. It can be seen that the proposed approach (SHIM) yielded better results than previous approaches compared to the ground truth of both experts. For example, using the ground truth of the first expert, SHIM yields  $\bar{D} = 0.712$  and  $\bar{D} = 0.671$  for the HP1 $\alpha$  and DAPI channel, respectively. The other approaches yield values of  $\bar{D} \in [0.591, 0.666]$  and  $\bar{D} \in [0.477, 0.609]$ , thus SHIM leads to an improvement of 7% to 20% for HP1 $\alpha$  and 10% to 40% for DAPI. Using the ground truth of the second expert, the improvement is 4% to 23% for HP1 $\alpha$  and 7% to 98% for DAPI. Table 2 shows mean values  $\bar{H}$  and standard deviations  $\sigma_H$  of the Hausdorff distance  $H$  for foci in the HP1 $\alpha$  and DAPI channel as well as for all foci. Using the ground truth of the first expert, SHIM leads to an improvement of 6% to 15% for HP1 $\alpha$  and 15% to 44% for DAPI. Using the ground truth of the second expert, the improvement is 10% to 25% for HP1 $\alpha$  and 8% to 43% for DAPI. Depending on the ground truth data and the microscopy channel, either RA+GA or UDWT yield the second best result for  $\bar{D}$  and  $\bar{H}$ . Compared to each of the second best results for  $\bar{D}$ , SHIM leads to an improvement of 7% or 8% (for all foci, see third row in Table 1) using the ground truth of the first or second expert, respectively. Compared to each of the second best results for  $\bar{H}$ , SHIM leads to an improvement of 8% of 12% (for all foci, see third row in Table 2). Since manual 3D segmentation is difficult and the foci volumes are relatively small (e.g., compared to nucleus volumes), relatively small differences between the segmentation result and the ground truth significantly decrease  $D$ , and inter-observer variabilities of  $D \in [0.4, 0.75]$  are typical. For example, dilating a typical 3D segmentation result of a medium-sized focus (volume of 296 voxels)

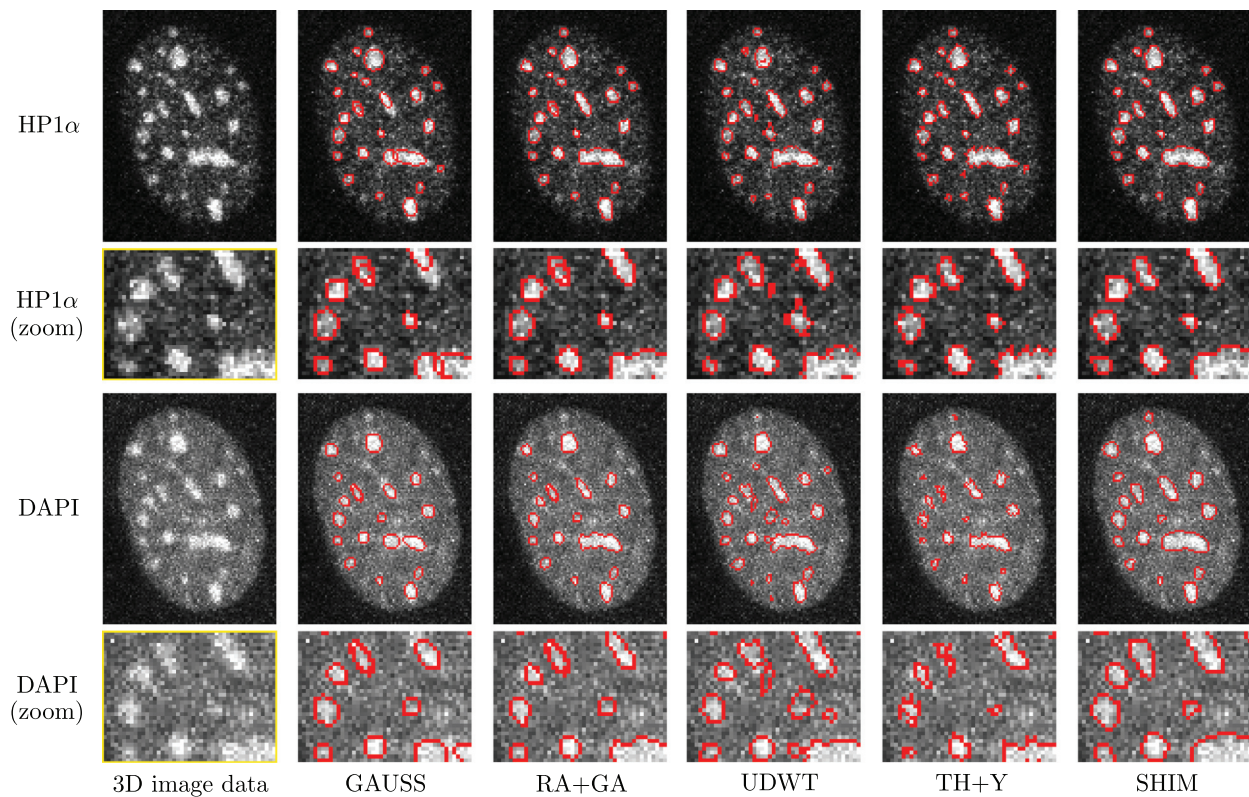


**Fig. 10.** Maximum intensity projections (MIPs) of original 3D image data (left), and 3D automatic segmentation results of previous approaches (GAUSS, RA+GA, UDWT, TH+Y), and the proposed 3D SH intensity model (SHIM).

**Table 1**

Quantitative comparison of different automatic approaches for 3D foci segmentation in real 3D microscopy images with ground truth from two different experts: Mean  $\bar{D}$  and standard deviation  $\sigma_D$  of the Dice coefficient. Larger values of  $\bar{D}$  are better, bold numbers highlight the best results.

		Inter-observer	Automatic vs. first expert					Automatic vs. second expert				
			GAUSS	RA+GA	UDWT	TH+Y	SHIM	GAUSS	RA+GA	UDWT	TH+Y	SHIM
HP1 $\alpha$ foci	$\bar{D}$	0.651	0.632	0.666	0.602	0.591	<b>0.712</b>	0.651	0.686	0.672	0.579	<b>0.713</b>
	$\sigma_D$	0.125	0.152	0.143	0.161	0.193	<b>0.101</b>	0.104	0.096	0.104	0.128	<b>0.075</b>
DAPI foci	$\bar{D}$	0.595	0.607	0.609	0.598	0.477	<b>0.671</b>	0.548	0.543	0.568	0.308	<b>0.610</b>
	$\sigma_D$	0.135	<b>0.116</b>	0.132	0.169	0.161	0.134	0.117	0.142	0.155	0.154	<b>0.116</b>
All foci	$\bar{D}$	0.625	0.621	0.640	0.600	0.556	<b>0.693</b>	0.599	0.614	0.619	0.475	<b>0.661</b>
	$\sigma_D$	0.132	0.137	0.140	0.164	0.190	<b>0.119</b>	0.122	0.141	0.142	0.192	<b>0.110</b>

**Table 2**

Quantitative comparison of different automatic approaches for 3D foci segmentation in real 3D microscopy images with ground truth from two different experts: Mean  $\bar{H}$  and standard deviation  $\sigma_H$  of the Hausdorff distance. Smaller values are better, bold numbers highlight the best results.

		Inter-observer	Automatic vs. first expert					Automatic vs. second expert				
			GAUSS	RA+GA	UDWT	TH+Y	SHIM	GAUSS	RA+GA	UDWT	TH+Y	SHIM
HP1 $\alpha$ foci	$\bar{H}$	3.569	4.278	3.852	4.275	4.090	<b>3.635</b>	3.342	2.854	2.755	3.030	<b>2.490</b>
	$\sigma_H$	2.878	3.344	<b>3.194</b>	3.362	3.344	3.351	1.926	1.421	1.316	1.353	<b>0.848</b>
DAPI foci	$\bar{H}$	4.101	4.665	4.290	4.094	6.250	<b>3.487</b>	5.037	4.846	4.400	7.145	<b>4.065</b>
	$\sigma_H$	2.179	2.848	2.656	2.528	8.184	<b>1.926</b>	2.829	2.462	2.174	6.326	<b>2.056</b>
All foci	$\bar{H}$	3.815	4.449	4.048	4.194	4.759	<b>3.568</b>	4.202	3.857	3.590	4.616	<b>3.289</b>
	$\sigma_H$	2.581	3.126	2.959	3.002	5.372	<b>2.780</b>	2.563	2.242	1.977	4.512	<b>1.762</b>

by 1 voxel and comparing the dilated result with the original result yields  $D = 0.493$ . In our experiments, the mean inter-observer variability for HP1 $\alpha$  and DAPI was  $\bar{D} = 0.651$  and  $\bar{D} = 0.595$ , respectively (see Table 1, third column). Thus, the results of SHIM are in the range of the inter-observer variability or even better. Analogously, the same holds true for the Hausdorff distance  $H$ . The computation time of our approach (implemented in C/C++) depends on the number of foci, the size of the ROI for model fitting, and the number of model parameters (which depends on  $l_{max}$ ).

For example, for a 3D two-channel image ( $512 \times 512 \times 41$  voxels) with 554 foci (both channels) in 8 cell nuclei, the computation time was about 3 min on an Intel Xeon CPU (2.67 GHz) running Linux.

### 5.2.2. Segmentation and shape analysis of heterochromatin foci in a knockout experiment

We also applied our approach to real 3D image data of a gene knockout study on how the Suv4-20h1/h2 histone methyl

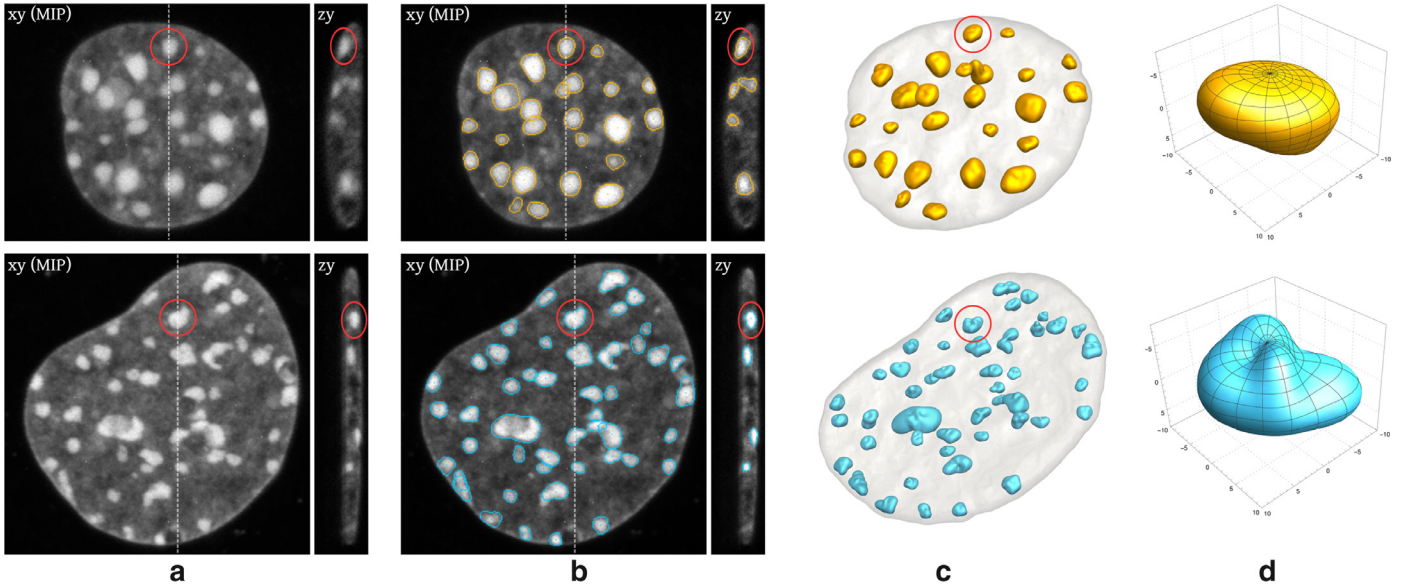


**Fig. 11.** Results of 3D foci segmentation using the proposed 3D SH intensity model (SHIM) for a wild-type nucleus (top) and a Suv4-20h1/h2 double-knockout nucleus (bottom): (a) Original 3D image data shown as maximum intensity projections (MIPs), (b) contour overlays of the 3D SH intensity model shown as MIPs, (c) rendering of the 3D shapes of the fitted models, (d) enlarged rendering of the 3D shapes of the foci marked by the circles in (a)-(c).

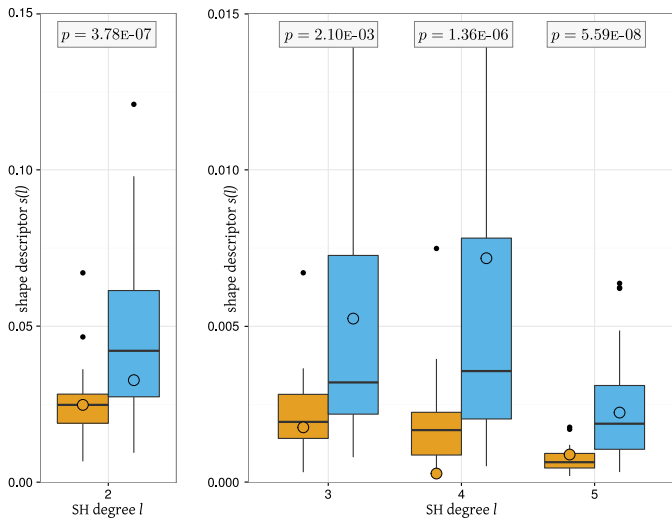


**Fig. 12.** Results of 3D foci shape analysis: Box plots of the computed shape descriptor  $s(l)$  for different SH degrees  $l = 2, 3, 4, 5$  of all segmented foci shown in Fig. 11c. For each degree  $l$ , results for the wild-type nucleus are represented by the left box (orange) and results for the double-knockout nucleus are represented by the right box (blue). The values marked with a circle indicate the values of  $s(l)$  of the two foci shown in Fig. 11d. (For interpretation of the references to color in this figure legend, the reader is referred to the web version of this article.)

transferases influence the structure of heterochromatin. A total of 17 3D microscopy images of mouse cells were analyzed using fixed segmentation parameters (and  $l_{\max} = 5$ ): 8 images of wild-type nuclei and 9 images of Suv4-20h1/h2 double-knockout nuclei (3–5 nuclei per image, image size of  $1024 \times 1024 \times 48$  to  $1024 \times 1024 \times 82$  voxels). Visual inspection of the image data by biological experts indicated that foci in some of the knockout nuclei have a more complex 3D shape than foci in wild-type nuclei. Fig. 11 shows examples of the image data as well as 3D segmentation results for one wild-type and one knockout nucleus, where such shape differences have been observed. It can be seen that the foci were well segmented and their 3D shape is captured well by the 3D SH intensity model. For the same nuclei, quantitative results of the shape descriptor  $s(l)$  for different SH degrees

$l = 2, 3, 4, 5$  are shown as box plots in Fig. 12. In agreement with the observations of the experts, the quantified values of  $s(l)$  are larger for the knockout nucleus (right boxes) than for the wild-type (left boxes). To determine whether the difference between the two distributions of  $s(l)$  is statistically significant, we ranked the shape descriptor samples to account for the non-normality of the distributions, and conducted a Welch's  $t$ -test (unequal variances  $t$ -test) for each degree  $l$ . The test showed that for  $l = 2, 3, 4, 5$  the difference between the average values of  $s(l)$  of the wild-type and knockout nucleus is significant ( $p$ -values of  $3.78e-07$ ,  $2.10e-03$ ,  $1.36e-06$ , and  $5.59e-08$ ).

### 5.3. Real 3D dynamic microscopy image data

In addition, we applied our approach to nine 3D dynamic time-lapse image sequences of mouse embryonic fibroblast cell nuclei (image size of  $150 \times 150 \times 59$  to  $150 \times 150 \times 101$  voxels, 10 minutes time interval, 15 to 90 time steps). Despite the relatively high level of image noise, we obtained good segmentation results using fixed parameters for all time steps of an image sequence (we used  $l_{\max} = 4$ ). As an example, Fig. 13 shows 3D segmentation results for a cell nucleus at four consecutive time steps. Note that the very small marked regions (e.g., for  $t = 13$  and  $t = 16$ ) correspond to topmost or lowermost planes of a segmented focus. To analyze 3D shape changes over time, we computed the shape descriptor  $s(l)$  in (20) based on the 3D segmentation result. Fig. 14 shows renderings of the 3D shapes of two foci marked by the circles at time step  $t = 13$  in Fig. 13 (top) and corresponding values of the shape descriptor  $s(l)$  for different SH degrees  $l = 2, 3, 4$  (bottom). The shape of the focus in the first row (red) is sphere-like and undergoes minor changes over time. Thus,  $s(l)$  is relatively constant. The elongation of the focus at time steps 6 to 7 and time steps 11 to 14 is reflected by an increase of  $s(2)$ . The shape of the focus in the second row (blue) is more complex (irregular) and undergoes significant changes. This is well reflected by  $s(3)$  and  $s(4)$ , for example, in time steps 12 to 17 where the shape of the focus evolves towards a sphere-like shape. This suggests that the shape descriptor can be exploited to analyze shape changes in 3D time-lapse image data.

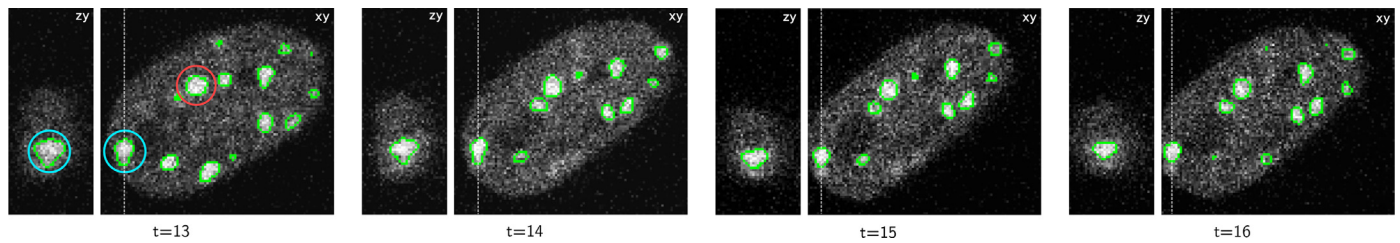


**Fig. 13.** Results of 3D foci segmentation for real 3D dynamic microscopy image data using the proposed 3D SH intensity model (SHIM): Cross sectional views (xy- and zy-planes) at four consecutive time steps  $t$  of the original 3D images overlaid with contours of the 3D segmentation result.

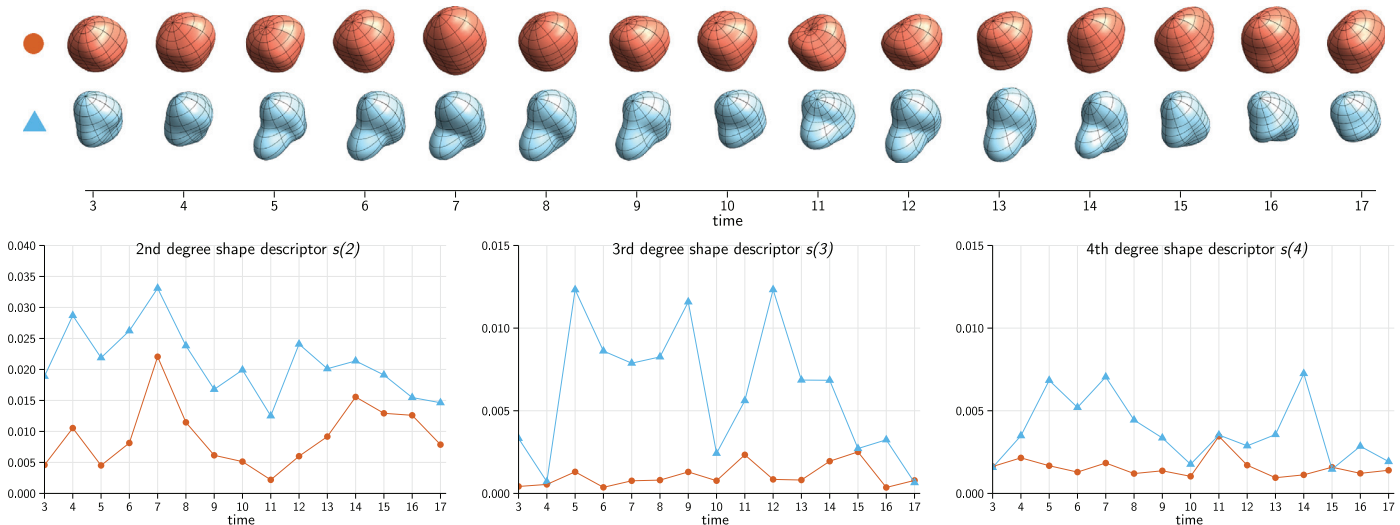


**Fig. 14.** Renderings of the 3D shape of heterochromatin foci (top) from real 3D dynamic microscopy image data as well as values of the shape descriptor  $s(l)$  (bottom) for different degrees  $l = 2$  (left),  $l = 3$  (center), and  $l = 4$  (right) as a function of time.

## 6. Conclusion

We have introduced a 3D model-based approach for automatic 3D segmentation of pericentric heterochromatin foci from 3D confocal light microscopy images. Our approach employs a novel 3D parametric intensity model based on a spherical harmonics (SH) expansion which analytically describes the 3D shape and intensities of the foci. To perform 3D foci segmentation, the 3D SH intensity model is directly fitted to the image intensities by solving a least-squares minimization problem. We have also presented an approach for 3D shape analysis of heterochromatin foci based on the segmentation result. To this end, a rotationally invariant shape descriptor is determined from the SH coefficients and used to characterize the 3D shape of the foci. For automatic determination of the 3D region-of-interest (ROI) for model fitting, we have presented a Hessian-based multiscale approach. We have also presented an approach for automatic initialization of the 3D SH intensity model. Our approach has been applied to synthetic 3D image data as well as to real 3D static and real 3D dynamic microscopy images. We have also performed a quantitative comparison with previous approaches. Our results for 3D synthetic image data demonstrate that the proposed approach copes better with the irregular 3D shapes of pericentric heterochromatin foci than previous model-based approaches for regular-shaped structures, and yields better results than previous non-model-based approaches, particularly for high levels of image noise. From our experimental results based on real 3D image data, it turned out that the proposed approach yields accurate results compared to ground truth and outperforms previous approaches. A main reason is that the SH expansion allows a more accurate 3D shape representation compared to previous model-based approaches using parametric

intensity models. At the same time, exploitation of a priori knowledge about the shape and intensity of heterochromatin structures improves the robustness to image noise and low foci contrast compared to non-model-based approaches. Our results for real 3D image data illustrate how different biological questions can be addressed using our approach:

- (1) It enables accurate 3D segmentation of heterochromatin and associated proteins (Fig. 10). For example, in contrast to HP1 $\alpha$  studied here, HP1 $\beta$  was found to localize differently with respect to heterochromatin (Mattout et al., 2015). Such differences can be quantified based on the 3D segmentation results of our approach.
- (2) 3D shape properties of heterochromatin foci can be quantified to assess the effect of chromatin modifiers, for example, the histone methylase Suv4-20h1/2 (Figs. 11 and 12).
- (3) Shape changes of heterochromatin foci over time can be quantified from dynamic 3D microscopy images (Figs. 13 and 14) and exploited to measure the kinetics of heterochromatin reorganization. Such experiments are essential to test predictions of theoretical mechanistic models that describe how epigenetic networks establish heterochromatin mediated gene silencing in systems biology studies (Müller-Ott et al., 2014).

A limitation of our approach is that it assumes homogeneity of foreground and background intensities of the foci. If these assumptions are not met, for example, for foci located at the nucleus border, where several background intensities exist in the local neighborhood of the foci, the accuracy of model fitting is reduced. Our approach also assumes a relatively uniform blurring of the image intensities in all directions, which is the case in our 3D image data.

For other image data with highly non-uniform blurring, for example, significantly higher blurring in z-direction, our approach could be extended. Another issue is the choice of the maximum degree of the SH expansion. In our experiments we used values smaller or equal to five. For very large foci, for example, in microscopy images with a higher spatial resolution, using values larger than five could yield more accurate results, since more shape details are visible and can be captured. A topic of future work is the automatic selection of an optimal value for the maximum degree of the SH expansion based on the 3D image data. In future work, we will also apply our approach to different types of 3D image data.

### Acknowledgment

This work was supported by the projects EpiSys (0315502) and CancerTelSys (01ZX1302) in the SysTec and e:Med programs of the German Federal Ministry of Education and Research (BMBF). We thank Dr. Qin Zhang (DKFZ Heidelberg, BioQuant, Division of Theoretical Systems Biology) for providing ground truth segmentation results.

### Appendix A. associated Legendre polynomials

The associated Legendre polynomials are defined by (e.g., (Arfken et al., 2005))

$$P_l^m(x) = \frac{(-1)^m}{2^l l!} (1-x^2)^{\frac{m}{2}} \frac{\partial^{l+m}}{\partial x^{l+m}} (x^2-1)^l \quad (\text{A.1})$$

To compute function values and first order derivatives of  $P_l^m(x)$ , we used the method described in Holmes and Featherstone (Holmes et al., 2002).

### Appendix B. first order partial derivatives of the 3D spherical harmonics intensity model

The first order partial derivatives of the SH intensity model  $g_{M, SH}(\mathbf{x}, \mathbf{p})$  (see (11) in Section 2.2) with respect to the model parameters  $\mathbf{p} = (\mathbf{a}, \mathbf{b}, a_0, a_1, \sigma, \mathbf{x}_0)^T$  are given by

$$\frac{\partial g_{M, SH}}{\partial a_1^m} = (a_1 - a_0) \left( G_\sigma(\mathcal{T}_1) \cos(m\varphi_\pi) N_l^m P_l^m(\cos \theta_\pi) + G_\sigma(\mathcal{T}_2) \cos(m\varphi) N_l^m P_l^m(\cos \theta) \right) \quad (\text{B.1})$$

$$\frac{\partial g_{M, SH}}{\partial b_1^m} = (a_1 - a_0) \left( G_\sigma(\mathcal{T}_1) \sin(m\varphi_\pi) N_l^m P_l^m(\cos \theta_\pi) + G_\sigma(\mathcal{T}_2) \sin(m\varphi) N_l^m P_l^m(\cos \theta) \right) \quad (\text{B.2})$$

$$\frac{\partial g_{M, SH}}{\partial a_0} = 1 - g_{SH}(\mathbf{h}, \mathbf{p}) \quad (\text{B.3})$$

$$\frac{\partial g_{M, SH}}{\partial a_1} = g_{SH}(\mathbf{h}, \mathbf{p}) \quad (\text{B.4})$$

$$\frac{\partial g_{M, SH}}{\partial \sigma} = \frac{a_1 - a_0}{\sigma} \left( \mathcal{T}_2 G_\sigma(\mathcal{T}_2) - \mathcal{T}_1 G_\sigma(\mathcal{T}_1) \right) \quad (\text{B.5})$$

$$\frac{\partial g_{M, SH}}{\partial x_0} = (a_1 - a_0) \left( \frac{\partial \mathcal{T}_1}{\partial x_0} G_\sigma(\mathcal{T}_1) - \frac{\partial \mathcal{T}_2}{\partial x_0} G_\sigma(\mathcal{T}_2) \right) \quad (\text{B.6})$$

analogous for  $\frac{\partial g_{M, SH}}{\partial y_0}, \frac{\partial g_{M, SH}}{\partial z_0}$

where  $\mathbf{h} = (h_x, h_y, h_z)^T$  denotes the relative 3D position with respect to  $\mathbf{x}_0 = (x_0, y_0, z_0)^T$ , i.e.,  $\mathbf{h} = \mathbf{x} - \mathbf{x}_0$ , and

$$\mathcal{T}_1 = r + r_{SH}(\theta_\pi, \varphi_\pi) \quad (\text{B.7})$$

$$\mathcal{T}_2 = r - r_{SH}(\theta, \varphi) \quad (\text{B.8})$$

$$\frac{\partial \mathcal{T}_1}{\partial x_0} = \frac{\partial r}{\partial x_0} + \frac{\partial}{\partial x_0} r_{SH}(\theta_\pi, \varphi_\pi) \quad (\text{B.9})$$

$$\frac{\partial \mathcal{T}_2}{\partial x_0} = \frac{\partial r}{\partial x_0} - \frac{\partial}{\partial x_0} r_{SH}(\theta, \varphi) \quad (\text{B.10})$$

$$\theta_\pi = \pi - \theta \quad (\text{B.11})$$

$$\varphi_\pi = \varphi + \pi \quad (\text{B.12})$$

$$G_\sigma(x) = \frac{1}{\sqrt{2\pi}\sigma} e^{-\frac{x^2}{2\sigma^2}}. \quad (\text{B.13})$$

To solve (B.9) and (B.10), the first order partial derivative of the radius function  $r_{SH}(\theta, \varphi)$  in (5) is required:

$$\begin{aligned} \frac{\partial r_{SH}(\theta, \varphi)}{\partial x_0} = & \sum_{l=0}^{l_{\max}} \left[ -\sin(\theta) a_l^0 N_l^0 \frac{\partial P_l^0(\cos \theta)}{\partial x_0} \frac{\partial \theta}{\partial x_0} \right. \\ & + \sum_{m=1}^l \left( m N_l^m P_l^m(\cos \theta) \frac{\partial \varphi}{\partial x_0} \right. \\ & \times (-a_l^m \sin(m\varphi) + b_l^m \cos(m\varphi)) \\ & - \sin(\theta) N_l^m \frac{\partial P_l^m(\cos \theta)}{\partial x_0} \frac{\partial \theta}{\partial x_0} \\ & \left. \left. \times (a_l^m \cos(m\varphi) + b_l^m \sin(m\varphi)) \right) \right]. \quad (\text{B.14}) \end{aligned}$$

Note that  $r = r(\mathbf{x})$ ,  $\theta = \theta(\mathbf{x})$ , and  $\varphi = \varphi(\mathbf{x})$  depend on  $\mathbf{x}_0$  (see (7)). The terms in (B.9), (B.10), and (B.14) are given by

$$\frac{\partial r}{\partial x_0} = -\frac{h_x}{r}, \text{ analogous for } \frac{\partial r}{\partial y_0}, \frac{\partial r}{\partial z_0} \quad (\text{B.15})$$

$$\frac{\partial \theta}{\partial x_0} = \frac{-h_x h_z}{r(\mathbf{h})^3} \left[ 1 - \left( \frac{h_z}{r(\mathbf{h})} \right)^2 \right]^{-\frac{1}{2}} \quad (\text{B.16})$$

$$\frac{\partial \theta}{\partial y_0} = \frac{-h_y h_z}{r(\mathbf{h})^3} \left[ 1 - \left( \frac{h_z}{r(\mathbf{h})} \right)^2 \right]^{-\frac{1}{2}} \quad (\text{B.17})$$

$$\frac{\partial \theta}{\partial z_0} = \left( \frac{1}{r(\mathbf{h})} - \frac{h_z^2}{r(\mathbf{h})^3} \right) \left[ 1 - \left( \frac{h_z}{r(\mathbf{h})} \right)^2 \right]^{-\frac{1}{2}} \quad (\text{B.18})$$

$$\frac{\partial \varphi}{\partial x_0} = \frac{h_y}{h_x^2 + h_y^2} \quad (\text{B.19})$$

$$\frac{\partial \varphi}{\partial y_0} = \frac{-h_x}{h_x^2 + h_y^2} \quad (\text{B.20})$$

$$\frac{\partial \varphi}{\partial z_0} = 0 \quad (\text{B.21})$$

## References

- Andrey, P., Kieu, K., Kress, C., Lehmann, G., Tirichine, L., Liu, Z., Biot, E., Adenot, P.-G., Hue-Beauvais, C., Houba-Herlin, N., Duranthon, V., Devino, E., Beaujean, N., Gaudin, V., Maurin, Y., Debey, P., 2010. Statistical analysis of 3D images detects regular spatial distributions of centromeres and chromocenters in animal and plant nuclei. *PLoS Comput. Bio.* 6 (7), e1000853.
- Arfken, G.B., Weber, H.J., Harris, F.E., 2005. *Mathematical methods for Physicists*, sixth Academic Press.
- Böcker, W., Iliakis, G., 2006. Computational methods for analysis of foci: validation for radiation-induced  $\gamma$ -H2AX foci in human cells. *Radiat. Res.* 165 (1), 113–124.
- Baust, M., Navab, N., 2010. A spherical harmonics shape model for level set segmentation. In: Daniilidis, K., Maragos, P., Paragios, N. (Eds.), *Proceedings of the 11th European Conference on Computer Vision (ECCV'10)*. In: *Lecture Notes in Computer Science*, 6313. Springer Berlin Heidelberg, Heraklion, Crete, Greece, pp. 580–593.
- Beil, M., Dürschmied, D., Paschke, S., Schreiner, B., Nolte, U., Bruel, A., Irinopolou, T., 2002. Spatial distribution patterns of interphase centromeres during retinoic acid-induced differentiation of promyelocytic leukemia cells. *Cytometry A* 47 (4), 217–225.
- Beil, M., Fleischer, F., Paschke, S., Schmidt, V., 2005. Statistical analysis of the three-dimensional structure of centromeric heterochromatin in interphase nuclei. *J. Microsc.* 217 (1), 60–68.
- Brechbühler, C., Gerig, G., Kübler, O., 1995. Parametrization of closed surfaces for 3-d shape description. *Comput. Vis. Image Underst.* 61 (2), 154–170.
- Cantaloube, S., Romeo, K., Le Baccon, P., Almouzni, G., Quivy, J.-P., 2012. Characterization of chromatin domains by 3D fluorescence microscopy: an automated methodology for quantitative analysis and nuclei screening. *BioEssays* 34 (6), 509–517.
- Courant, R., Hilbert, D., 1953. *Methods of Mathematical Physics*, second Interscience.
- Cremer, T., Cremer, M., Hübner, B., Strickfaden, H., Smeets, D., Popken, J., Sterr, M., Markaki, Y., Rippe, K., Cremer, C., 2015. The 4D nucleome: evidence for a dynamic nuclear landscape based on co-aligned active and inactive nuclear compartments. *FEBS Lett.* doi:10.1016/j.febslet.2015.05.037.
- de Chaumont, F., Dallongeville, S., Chenouard, N., Hervé, N., Pop, S., Provoost, T., Meas-Yedid, V., Pankajakshan, P., Lecomte, T., Le Montagner, Y., Lagache, T., Dufour, A., Olivo-Marin, J.-C., 2012. Icy: An open bioimage informatics platform for extended reproducible research. *Nature Methods* 9 (7), 690–696.
- Du, C.-J., Hawkins, P.T., Stephens, L.R., Bretschneider, T., 2013. 3d time series analysis of cell shape using laplacian approaches. *BMC Bioinform.* 14 (296).
- Ducroz, C., Olivo-Marin, J.-C., Dufour, A., 2012. Characterization of cell shape and deformation in 3d using spherical harmonics. In: Frangi, A., Santos, A. (Eds.), *Proceedings of the 9th IEEE Internat. Symposium on Biomedical Imaging: From Nano to Macro (ISBI'12)*. IEEE Computer Society, Barcelona, Spain, pp. 848–851.
- Dzyubachyk, O., Essers, J., van Cappellen, W.A., Baldeyron, C., Inagaki, A., Niessen, W.J., Meijering, E., 2010. Automated analysis of time-lapse fluorescence microscopy images: from live cell images to intracellular foci. *Bioinform.* 26 (19), 2424–2430.
- Eck, S., Rohr, K., Müller-Ott, K., Rippe, K., Wörz, S., 2012. Combined model-based and region-adaptive 3D segmentation and 3D co-localization analysis of heterochromatin foci. In: Tolxdorff, T., Deserno, T., Handels, H., Meinzer, H.-P. (Eds.), *Proceedings on Workshop of Bildverarbeitung für die Medizin (BVM'12)*. In: *Informatik aktuell*. Springer Berlin Heidelberg, Berlin, Germany, pp. 9–14.
- Eck, S., Rohr, K., Biesdorf, A., Müller-Ott, K., Rippe, K., Wörz, S., 2013. A 3D intensity model based on spherical harmonics for automatic 3D segmentation of heterochromatin foci. In: Parvin, C., Viergever, M., Liebling, M., Staib, S. (Eds.), *Proceedings of the 10th IEEE Internat. Symposium on Biomedical Imaging: From Nano to Macro (ISBI'13)*. IEEE Computer Society, San Francisco, CA/USA, pp. 1476–1479.
- Eck, S., Wörz, S., Müller-Ott, K., Hahn, M., Schotta, G., Rippe, K., Rohr, K., 2014. 3d shape analysis of heterochromatin foci based on a 3d spherical harmonics intensity model. In: Ourselin, S., Styner, M. (Eds.), *Proceedings of the SPIE Medical Imaging 2014: Image Processing*. In: *Proceedings of SPIE*, 9034. SPIE Bellingham, WA/USA, San Diego, CA/USA, pp. 1484–1487.
- El-Baz, A., Nitzken, M., Khalifa, F., Elnakib, A., Gimel'farb, G., Falk, R., El-Ghar, M., 2011. 3d shape analysis for early diagnosis of malignant lung nodules. In: Székely, G., Hahn, H. (Eds.), *Proceedings of the 22nd Internat. Conf. on Information Processing in Medical Imaging (IPMI'11)*. In: *Lecture Notes in Computer Science*, 6801. Springer Berlin Heidelberg, Kloster Irsee, Germany, pp. 772–783.
- Frangi, A.F., Niessen, W.J., Vincken, K.L., Viergever, M.A., 1998. Multiscale vessel enhancement filtering. In: Wells, W., Colchester, A., Delp, S. (Eds.), *Proceedings of the First Internat. Conf. on Medical Image Computing and Computer-Assisted Intervention (MICCAI'98)*. In: *Lecture Notes in Computer Science*, 1496. Springer Berlin Heidelberg, Cambridge, MA/USA, pp. 130–137.
- Gerig, G., Styner, M., Jones, D., Weinberger, D., Lieberman, J., 2001. Shape analysis of brain ventricles using SPHARM. In: Staib, L. (Ed.), *Proceedings in the Workshop on Mathematical Methods in Biomedical Image Analysis 2001 (MMBIA'01)*. Kauai, HI/USA, pp. 171–178.
- Gu, X., Wang, Y., Chan, T.F., Thompson, P.M., Yau, S., 2004. Genus zero surface conformal mapping and its application to brain surface mapping. *IEEE Trans. Med. Imaging* 23 (8), 949–958.
- Hahn, M., Dambacher, S., Schotta, G., 2010. Heterochromatin dysregulation in human diseases. *J. Appl. Physiol.* 109 (1), 232–242.
- Hahn, M., Dambacher, S., Dulev, S., Kuznetsova, A.Y., Eck, S., Wörz, S., Sadic, D., Schulte, M., Mallm, J.-P., Maiser, A., Debs, P., von Melchner, H., Leonhardt, H., Schermelleh, L., Rohr, K., Rippe, K., Storchova, Z., Schotta, G., 2013. Suv4-20h2 mediates chromatin compaction and is important for cohesin recruitment to heterochromatin. *Genes Dev.* 27 (8), 859–872.
- Hathaway, N.A., Bell, O., Hodges, C., Miller, E.L., Neel, D.S., Crabtree, G.R., 2012. Dynamics and memory of heterochromatin in living cells. *Cell* 149 (7), 1447–1460.
- Holmes, S.A., Featherstone, W.E., 2002. A unified approach to the clenshaw summation and the recursive computation of very high degree and order normalised associated legendre functions. *J. Geodesy* 76 (5), 279–299.
- Horáková, A.H., Bártová, E., Galiová, G., Uhlířová, R., Matula, P., Kozubek, S., 2010. Suv39h-independent association of hp1 beta with fibrillarin-positive nucleolar regions. *Chromosoma* 119 (3), 227–241.
- Ivashkevich, A.N., Martin, O.A., Smith, A.J., Redon, C.E., Bonner, W.M., Martin, R.F., Lobachevsky, P.N., 2011. H2AX foci as a measure of DNA damage: a computational approach to automatic analysis. *Mutat. Res.* 711 (1-2), 49–60.
- Jaeger, S., Palaniappan, K., Casas-Delucchi, C.S., Cardoso, M.C., 2010. Classification of cell cycle phases in 3d confocal microscopy using PCNA and chromocenter features. In: Chellappa, R., Anandan, P., Rajagopalan, A., Narayanan, P.J., Torr, P.H.S. (Eds.), *Proceedings of the 7th Indian Conference on Computer Vision, Graphics and Image Processing (ICVGIP '10)*. Chennai, India, pp. 412–418.
- Jost, K.L., Haase, S., Smeets, D., Schrode, N., Schmiel, J.M., Bertulat, B., Herzell, H., Cremer, M., Cardoso, M.C., 2011. 3D-image analysis platform monitoring relocation of pluripotency genes during reprogramming. *Nucleic Acids Res.* 39 (17), e113.
- Kazhdan, M., Funkhouser, T., Rusinkiewicz, S., 2003. Rotation invariant spherical harmonic representation of 3d shape descriptors. In: Kobbelt, L., Schröder, P., Hoppe, H. (Eds.), *Proceedings of the Eurographics Symposium on Geometry Processing (SGP'03)*. The Eurographics Association, Aachen, Germany, pp. 156–164.
- Kelemen, A., Reist, H.-W., Gerig, G., Székely, G., 1996. Automatic segmentation of cell nuclei from confocal laser scanning microscopy images. In: Höhne, K.H., Kikinis, R. (Eds.), *Proceedings of the Visualization in Biomedical Computing (VBC'96)*. In: *Lecture Notes in Computer Science*. Springer, Hamburg, Germany, pp. 193–202.
- Kelemen, A., Székely, G., Gerig, G., 1999. Elastic model-based segmentation of 3-d neuroradiological data sets. *IEEE Trans. Med. Imaging* 18 (10), 828–839.
- Khairy, K., Foo, J., Howard, J., 2010. Shapes of red blood cells: Comparison of 3d confocal images with the bilayer-couple model. *Cell. Mol. Bioeng.* 1 (2-3), 173–181.
- Müller, K.P., Erdel, F., Caudron-Herger, M., Marth, C., Fodor, B.D., Richter, M., Scarnaro, M., Beaudouin, J., Wachsmuth, M., Rippe, K., 2009. Multiscale analysis of dynamics and interactions of heterochromatin protein 1 by fluorescence fluctuation microscopy. *Biophys. J.* 97 (11), 2876–2885.
- Müller-Ott, K., Erdel, F., Matveeva, A., Mallm, J.-P., Rademacher, A., Hahn, M., Bauer, C., Zhang, Q., Kaltofen, S., Schotta, G., Höfer, T., Rippe, K., 2014. Specificity, propagation, and memory of pericentric heterochromatin. *Mol. Syst. Bio.* 10 (8), 1–22.
- Marquardt, D., 1963. An algorithm for least-squares estimation of nonlinear parameters. *J. Soc. Ind. Appl. Math.* 11 (2), 431–441.
- Marshall, W.F., Dernburg, A.F., Harmon, B., Agard, D.A., Sedat, J.W., 1996. Specific interactions of chromatin with the nuclear envelope: positional determination within the nucleus in *Drosophila melanogaster*. *Mol. Cell* 7 (5), 825–842.
- Mattout, A., Aaronson, Y., Sailaja, B.S., Raghu Ram, E.V., Harikumar, A., Mallm, J.-P., Sim, K.H., Nissim-Rafinia, M., Supper, E., Singh, P.B., Sze, S.K., Gasser, S.M., Rippe, K., Meshorer, E., 2015. Heterochromatin protein 1 $\beta$  (HP1 $\beta$ ) has distinct functions and distinct nuclear distribution in pluripotent versus differentiated cells. *Genome Bio.* 16 (1), 213.
- Matula, P., Verissimo, F., Wörz, S., Eils, R., Pepperkok, R., Rohr, K., 2010. Quantification of fluorescent spots in time series of 3-D confocal microscopy images of endoplasmic reticulum exit sites based on the HMAX transform. In: Dawant, B., Haynor, D. (Eds.), *In: Proceedings of SPIE Medical Imaging 2010: Image Processing*. Proceeding of SPIE, 7623. SPIE Bellingham, WA/USA, San Diego, CA/USA pp. 76261H-1–76261H-7.
- Meshorer, E., Yellajoshula, D., George, E., Scambler, P.J., Brown, D.T., Misteli, T., 2006. Hyperdynamic plasticity of chromatin proteins in pluripotent embryonic stem cells. *Dev. Cell* 10 (1), 105–116.
- Olivo-Marin, J.-C., 2002. Extraction of spots in biological images using multiscale products. *Pattern Recognit.* 35 (9), 1989–1996.
- Osterwald, S., Deeg, K.L., Chung, I., Parisotto, D., Wörz, S., Rohr, K., Erfle, H., Rippe, K., 2015. Pml induces compaction, trf2 depletion and dna damage signaling at telomeres and promotes their alternative lengthening. *J. Cell Sci.* 128 (10), 1887–1900.
- Pepperkok, R., Ellenberg, J., 2006. High-throughput fluorescence microscopy for systems biology. *Nat. Rev. Mol. Cell Bio.* 7 (9), 690–696.
- Plass, C., Pfister, S.M., Lindroth, A.M., Bogatyrova, O., Claus, R., Lichter, P., 2013. Mutations in regulators of the epigenome and their connections to global chromatin patterns in cancer. *Nat. Rev. Genet.* 14 (11), 765–780.
- Pop, S., Dufour, A.C., Le Garrec, J.-F., Ragni, C.V., Cimper, C., Meilhac, S.M., Olivo-Marin, J.-C., 2013. Extracting 3d cell parameters from dense tissue environments: Application to the development of the mouse heart. *Bioinform.* 29 (6), 772–779.
- Poulet, A., Arganda-Carreras, I., Legland, D., Probst, A.V., Andrey, P., Tatout, C., 2015. Nucleus: an image plugin for quantifying 3D images of interphase nuclei. *Bioinform.* 31 (7), 1144–1146.
- Probst, A.V., Almouzni, G., 2008. Pericentric heterochromatin: Dynamic organization during early development in mammals. *Differentiation* 76 (1), 15–23.

- Saab, B.J., Mansuy, I.M., 2014. Neurobiological disease etiology and inheritance: an epigenetic perspective. *J. Exp. Bio.* 217 (Pt 1), 94–101.
- Saksouk, N., Simboeck, E., Déjardin, J., 2015. Constitutive heterochromatin formation and transcription in mammals. *Epigenetics Chromatin* 8 (3), 1–17.
- Sexton, T., Cavalli, G., 2015. The role of chromosome domains in shaping the functional genome. *Cell* 160 (6), 1049–1059.
- Singh, S., Janoos, F., Pecot, T., Caserta, E., Huang, K., Rittscher, J., Leone, G., Machiraju, R., 2011. Non-parametric population analysis of cellular phenotypes. In: Fichtinger, G., Martel, A., Peters, T. (Eds.), *Proceedings of the 14th Internat. Conf. on Medical Image Computing and Computer-Assisted Intervention (MICCAI'11)*. In: *Lecture Notes in Computer Science*, 6891. Springer Berlin Heidelberg, Toronto, Canada, pp. 343–351.
- Styner, M., Lieberman, J.A., Pantazis, D., Gerig, G., 2004. Boundary and medial shape analysis of the hippocampus in schizophrenia. *Med. Image Anal.* 8 (3), 197–203.
- Székely, G., Kelemen, A., Brechbühler, C., Gerig, G., 1996. Segmentation of 2-d and 3-d objects from MRI volume data using constrained elastic deformations of flexible fourier contour and surface models. *Med. Image Anal.* 1 (1), 19–34.
- Thomann, D., Rines, D.R., Sorger, P.K., Danuser, G., 2002. Automatic fluorescent tag detection in 3d with super-resolution: application to the analysis of chromosome movement. *J. Microsc.* 208, 49–64.
- Tutar, I.B., Pathak, S.D., Gong, L., Cho, P.S., Wallner, K., Kim, Y., 2006. Semiautomatic 3-d prostate segmentation from TRUS images using spherical harmonics. *IEEE Trans. Med. Imaging* 25 (12), 1645–1654.
- Wörz, S., Rohr, K., 2006. Localization of anatomical point landmarks in 3d medical images by fitting 3d parametric intensity models. *Med. Image Anal.* 10 (1), 41–58.
- Wörz, S., Sander, P., Pfannmöller, M., Rieker, R.J., Joos, S., Mechttersheimer, G., Boukamp, P., Lichter, P., Rohr, K., 2010. 3D geometry-based quantification of colocalizations in multichannel 3D microscopy images of human soft tissue tumors. *IEEE Trans. Med. Imaging* 29 (8), 1474–1484.
- Waters, J.C., 2009. Accuracy and precision in quantitative fluorescence microscopy. *J. Cell Bio.* 185 (7), 1135–1148.
- Webster, A.L.H., Yan, M.S.-C., Marsden, P.A., 2013. Epigenetics and cardiovascular disease. *Can. J. Cardiol.* 29 (1), 46–57.
- Yen, J., Chang, F., Chang, S., 1995. A new criterion for automatic multilevel thresholding. *IEEE Trans. Image Process.* 4 (3), 370–378.